

Cross-shore surfzone tracer dispersion in an alongshore current

David B. Clark,¹ Falk Feddersen,¹ and R. T. Guza¹

Received 1 August 2009; revised 25 March 2010; accepted 27 April 2010; published 15 October 2010.

[1] Cross-shore surfzone tracer dispersion in a wave driven alongshore current is examined over a range of wave and current conditions with 6 continuous dye releases, each roughly 1–2 hours in duration, at Huntington Beach, California. Fluorescent dye tracer released near the shoreline formed shore parallel plumes that were sampled on repeated cross-shore transects with a jet ski mounted fluorometer. Ensemble averaged cross-shore tracer concentration profiles are generally shoreline attached (maximum at or near the shoreline), with increasing cross-shore widths and decreasing peak values with downstream distance. More than a few 100 m from the source, tracer is often well mixed across the surfzone (i.e., saturated) with decreasing tracer concentrations farther seaward. For each release, cross-shore surfzone absolute diffusivities are estimated using a simple Fickian diffusion solution with a no-flux boundary at the shoreline, and range from 0.5–2.5 m² s⁻¹. Surfzone diffusivity scalings based on cross-shore bore dispersion, surfzone eddy mixing length, and undertow driven shear dispersion are examined. The mixing-length scaling has correlation $r^2 = 0.59$ and the expected best-fit slope <1, indicating that horizontal rotational motions are important for cross-shore tracer dispersion in the surfzone.

Citation: Clark, D. B., F. Feddersen, and R. T. Guza (2010), Cross-shore surfzone tracer dispersion in an alongshore current, *J. Geophys. Res.*, 115, C10035, doi:10.1029/2009JC005683.

1. Introduction

[2] Beaches and the adjacent surfzone are used for recreational and commercial activities, and provide habitat to a variety of fish and benthic species. Beach related tourism provides yearly revenue of about 1 billion dollars in Los Angeles and Orange Counties, California, U.S.A. [Hanemann *et al.*, 2001]. These economic and environmental resources are threatened by polluted terrestrial runoff that frequently drains onto the shoreline where it is entrained and spread in the surfzone [Boehm *et al.*, 2002]. Waterborne pollution threatens public health, causing both gastrointestinal and upper respiratory symptoms in exposed beach goers [Haile *et al.*, 1999], and results in frequent beach closures [Noble *et al.*, 2000]. A model predicting the transport and dilution of surfzone pollutants would improve beach management. However, the processes that mix tracers within the surfzone are understood poorly.

[3] Fluorescent dye tracers have been used to investigate surfzone mixing and transport [Harris *et al.*, 1963; Inman *et al.*, 1971; Grant *et al.*, 2005; Clarke *et al.*, 2007]. Visually observed tracer patches initially dispersed cross-shore until the surfzone was saturated (approximately uniform cross-shore dye concentration), followed by dominant alongshore

dispersion [Harris *et al.*, 1963; Inman *et al.*, 1971; Clarke *et al.*, 2007]. After several hours, surfzone tracer patches were observed to stretch 5–8 km alongshore while remaining within a few surfzone widths of the shoreline [Grant *et al.*, 2005]. Seaward of the surfzone, visually slower dispersion suggested that mixing was weaker than within the surfzone.

[4] A wide range of field estimated surfzone diffusivities ($\kappa \sim 10^{-3}$ – 10^4 m² s⁻¹) have been found by fitting dye tracer data to Fickian diffusion solutions assuming constant alongshore currents and depth [Harris *et al.*, 1963; Inman *et al.*, 1971; Clarke *et al.*, 2007]. Harris *et al.* [1963] estimated alongshore diffusivity κ_{yy} by measuring dye concentrations from bottle samples collected at several shoreline locations during both point and continuous tracer releases. Inman *et al.* [1971] sampled point released dye with bottles at the shoreline and at the visually estimated dye patch center. Clarke *et al.* [2007] estimated diffusivities by fitting a 2-D advection diffusion solution to point dye releases that were bottle sampled at several shoreline locations.

[5] Cross-shore tracer structure was not observed in previous surfzone field studies [Harris *et al.*, 1963; Inman *et al.*, 1971; Clarke *et al.*, 2007]. Diffusivity estimates were derived from single realizations in space and time, without the ensemble averaging over plume and patch fluctuations needed for stability in diffusivity estimates [e.g., Csanady, 1973]. In addition, local waves and currents were generally not measured, complicating the interpretation of diffusivity parameterizations.

[6] Laboratory experiments using shore-normal monochromatic waves without [Harris *et al.*, 1963] and with

¹Integrative Oceanography Division, Scripps Institution of Oceanography, University of California San Diego, La Jolla, California, USA.

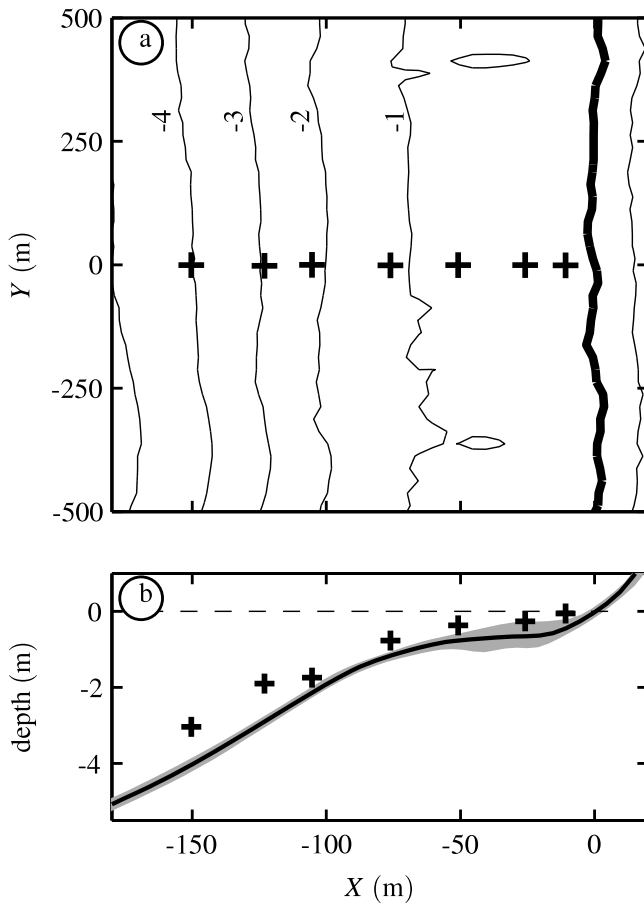


Figure 1. (a) Plan view of HB06 bathymetry (depth) contours versus cross-shore distance X from the MSL shoreline, and alongshore distance Y from the instrumented frames (black crosses). Thin curves are depth contours (labeled in m) and the thick black contour is at mean sea level (MSL). (b) Mean depth versus X , with depth equal to zero at the MSL shoreline (dashed black line). The gray region indicates the bathymetry standard deviation over Y and time, and black crosses indicate approximate vertical instrument locations.

[Pearson *et al.*, 2009] an imposed alongshore current have been used to study surfzone tracer dispersion. Harris *et al.* [1963] estimated a combined cross- and alongshore diffusivity κ , and used turbulent dissipation and an eddy length scale to derive a $\kappa \sim H_b^2 T_b^{-1}$ scaling, where H_b was the breaking wave height and T_b was the mean breaking wave period. Pearson *et al.* [2009] estimated a cross-shore diffusivity κ_{xx} from mean cross-shore dye profiles at several locations downstream from a continuous dye source, and proposed a cross-shore shear dispersion scaling using the sheared mean cross-shore current (undertow) and a vertical diffusivity.

[7] Using a shoreward propagating region of diffusivity to represent the mixing effects of a broken wave (bore), the effects of single and multiple waves on cross-shore tracer concentrations were investigated using numerical models [Feddersen, 2007]. A non-dimensional cross-shore average diffusivity $\hat{\kappa} = \sqrt{\pi}/(\hat{c}\hat{T})$ was derived where \hat{c} and \hat{T} are the

non-dimensional cross-shore wave speed and wave period [Feddersen, 2007; Henderson, 2007].

[8] Drifters have also been used to estimate surfzone diffusivities. On roughly alongshore uniform beaches, drifter estimated diffusivities were time-dependent with asymptotic (long-time) κ_{xx} between $0.5\text{--}1.5\text{ m}^2\text{ s}^{-1}$ and asymptotic κ_{yy} between $2\text{--}18\text{ m}^2\text{ s}^{-1}$ [Spydell *et al.*, 2007, 2009]. Good agreement was found between the asymptotic κ_{yy} and both mixing-length and shear dispersion scalings. At beaches with irregular bathymetry that control circulation (i.e., rip channels), estimated asymptotic diffusivities were $\kappa_{xx} = 0.9\text{--}2.2\text{ m}^2\text{ s}^{-1}$ and $\kappa_{yy} = 2.8\text{--}3.9\text{ m}^2\text{ s}^{-1}$ [Brown *et al.*, 2009], and estimated relative diffusivities were $\kappa_{xx} \approx -0.8\text{--}2\text{ m}^2\text{ s}^{-1}$ and $\kappa_{yy} = 1.8\text{--}4.8\text{ m}^2\text{ s}^{-1}$ [Johnson and Pattiarachi, 2004]. Unlike tracers, drifters duck under breaking waves and are not entrained in the front face of a bore. Diffusivities for drifters and tracers may differ.

[9] Here, field observations of continuously released surfzone dye tracer plumes in quasi-steady alongshore currents on generally alongshore uniform bathymetry are presented. Tracer experiments are conducted over a range of wave and current conditions (section 2.1). Dye released into the surfzone (section 2.2) is measured on repeated cross-shore transects by a dye sampling jet ski (section 2.3). Using ensemble (absolute) averaged cross-shore concentration profiles, cross-shore integrated tracer statistics are estimated (section 3). Variation in individual tracer profiles, the structure of mean profiles, and the downstream evolution of tracer profile statistics are described in section 4. A simple Fickian diffusion model for tracer released at the shoreline with a no-flux shoreline boundary (section 5.1) is used to estimate surfzone absolute κ_{xx} (section 5.2) from mean dye profiles that are well contained in the surfzone. The Fickian solution is compared with observed tracer moments (section 5.3). The observed surfzone κ_{xx} are compared with other surfzone κ_{xx} estimates (section 6.1), and inferences are made about the relative strength of mixing seaward of the surfzone (section 6.2). Three κ_{xx} scalings and related dispersion mechanisms are discussed (section 6.3), and the possible causes of decreased tracer transport between the dye release pump and downstream transects are examined (section 6.4). Section 7 is a summary.

2. HB06 Experiment

2.1. Field Site, Waves, and Currents

[10] The HB06 experiment took place from September 14th to October 17th, 2006 in Huntington Beach, California located 50 km south of Los Angeles. The approximately straight, 1 km long study beach faces 214° southwest. Off-shore islands strongly effect the incident waves by blocking shore-normal southwesterly swells, and obliquely incident waves from the west or south often drive strong alongshore currents.

[11] The X and Y coordinates are the cross-shore distance from the mean sea level (MSL) shoreline, and the alongshore distance from the instrumented transect (Figure 1), respectively. Bathymetry (Figure 1a) was surveyed three times on 42 cross-shore transects using a GPS equipped jet ski, ATV, and hand pushed cart [Seymour *et al.*, 2005]. The alongshore and time-averaged bathymetry slope is 0.03 seaward of about 2 m depth, decreases to 0.006 between roughly 0.7 m

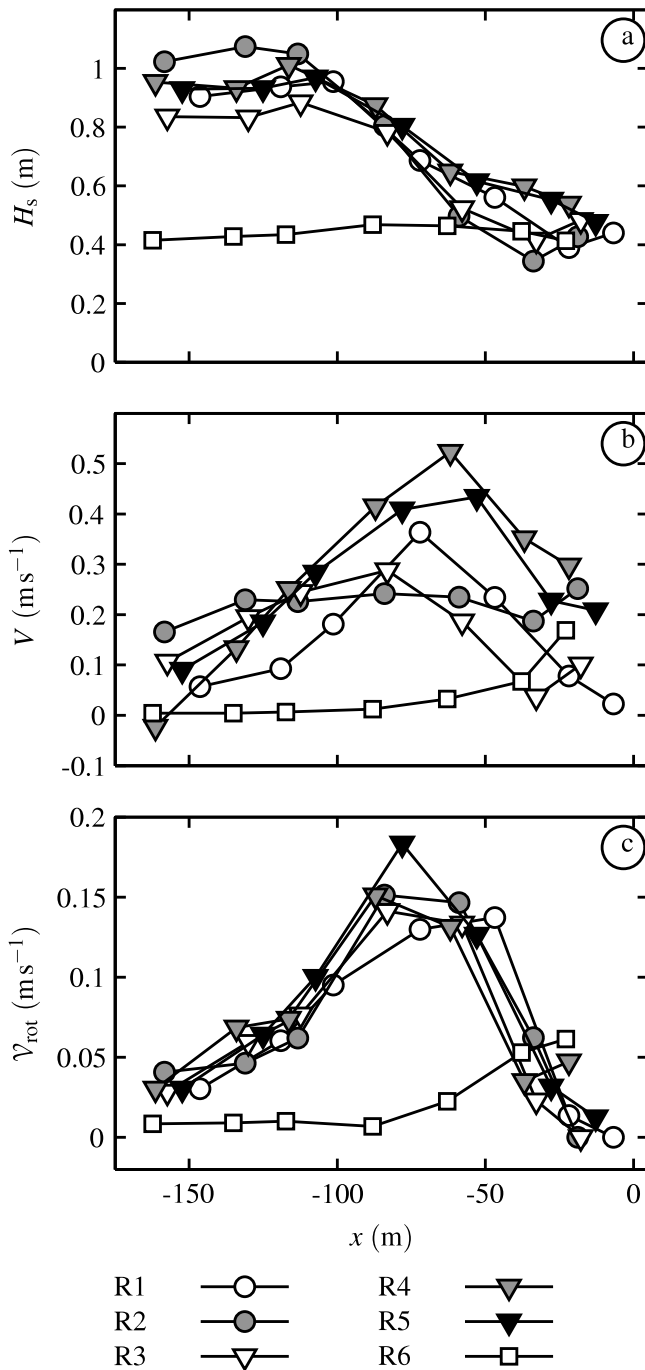


Figure 2. (a) Significant wave height H_s , (b) mean alongshore current V , and (c) horizontal rotational velocities V_{rot} versus cross-shore distance from the shoreline x for each dye release (see legend).

and 2 m depth, and steepens to 0.075 on the beach face (Figure 1b). Changes in the seaward portion of the bathymetry over time were small. However, a small trough near the shoreline early in the observations subsequently accreted (shaded region between $-50 < X < -10$ m in Figure 1b). The tidal range is typically less than ± 1 m.

[12] Seven tripod frames with pressure sensors and acoustic Doppler velocimeters (ADV) were deployed in a 140 m long cross-shore array from near the shoreline to 4 m

mean depth (Figure 1a). Frames are numbered from 1 (shallowest) to 7 (deepest). Frame 7 was always seaward of the surfzone. Frame 1 was 11 m from the MSL shoreline, and the ADV was out of the water during low tides.

[13] During the six HB06 dye release experiments (R1 through R6) the dominant south swell drove surfzone alongshore currents and dye in the $+Y$ (up coast) direction. For each dye release, x is the cross-shore distance from the mean shoreline (tide dependent), and y is the alongshore distance from the continuous dye source. Significant wave heights $H_s(x)$, alongshore currents $V(x)$, and horizontal (low-frequency) rotational velocities $V_{rot}(x)$ [Lippmann *et al.*, 1999] were measured at each frame (Figure 1) and averaged over the duration of each release (Figure 2 and Table 1). The $H_s(x)$ are estimated from pressure spectra (depth corrected to the surface) over the sea-swell band. Following Lippmann *et al.* [1999], low frequency vortical motions $V_{rot}(x)$ are estimated by removing irrotational infragravity wave energy from the observed velocity via

$$V_{rot}(x) = \sqrt{\int_{IG} (\tilde{u}^2 + \tilde{v}^2 - \frac{g}{h} \tilde{p}^2) df}, \quad (1)$$

where \tilde{u} , \tilde{v} , \tilde{p} are the cross-shore, alongshore, and pressure spectra respectively, f is frequency, and the integral is over the infragravity band ($0.004 < F < 0.03$ Hz). This $V_{rot}(x)$ estimate approximates shear wave velocity variance [Noyes *et al.*, 2002].

[14] For releases R1 through R5, $H_s(x)$ shoaled to a maximum near $x = -110$ m then decreased towards the shoreline as broken waves dissipated (Figure 2a). For R1–R5, $V(x)$ and $V_{rot}(x)$ had similar cross-shore structure with mid-surfzone maxima (Figures 2b and 2c). Wave heights during R6 were smaller than the other releases, reaching a maximum closer to the shoreline ($x = -88$ m), with a weak $H_s(x)$ decay towards the shoreline (Figure 2a). Unlike R1 through R5, R6 also had $V(x)$ and $V_{rot}(x)$ (Figures 2b and 2c) maxima close to the shoreline.

[15] Averaged over each release, the incident (Frame 7) H_s range from 0.41 to 1.02 m, mean wave periods T_m from 9.0 to 9.9 s (from energy weighted pressure spectra over the sea-swell band), incident wave angle (θ) from 0.9 to 9.8 degrees down coast (after significant shoaling and refraction), and directional spread from 14.6 to 23.1 degrees (Table 1). The surfzone width L_x is between 88 m and 122 m, with the seaward edge of the surfzone $x = -L_x$ defined as the cross-shore location of the H_s maximum (Table 1). Cross-shore averaging over the frames within the surfzone results in

Table 1. Wave and Current Statistics for Each Dye Release^a

Release	Date	H_s (m)	T_m (s)	θ (deg)	σ_θ (deg)	\bar{V} (ms^{-1})	\bar{V}_{rot} (ms^{-1})	L_x (m)
R1	Sep 18	0.90	9.5	9.8	14.6	0.18	0.075	101
R2	Sep 22	1.02	9.1	0.9	23.1	0.23	0.082	122
R3	Sep 28	0.84	9.9	7.8	17.8	0.21	0.073	112
R4	Sep 29 am	0.95	9.1	6.5	18.3	0.37	0.088	116
R5	Sep 29 pm	0.93	9.0	6.3	17.8	0.31	0.090	116
R6	Oct 11	0.41	9.2	7.0	15.3	0.07	0.036	88

^aRelease number, release date, incident (frame 7) mean significant wave height H_s , mean period T_m , wave angle θ , directional spread σ_θ , surfzone averaged mean alongshore current \bar{V} , surfzone averaged horizontal rotational velocity \bar{V}_{rot} , and surfzone width L_x are shown.

Table 2. Dye Sampling Parameters for Each Release^a

Release	Duration (min)	x_0 (m)	x_{in} (m)	Transects	$\langle N_j \rangle^{(j)}$	$\langle N_j \rangle^{(j)}$	τ_{decorr} (s)
R1	66	-54	-13	3	15.3	15.3	41
R2	40	-13	-11	5	9.8	7.5	64
R3	117	-10	-13	6	11.3	5.9	135 ^b
R4	64	-22	-17	8	4.5	4.4	79
R5	66	-4	-14	5	5.8	4.9	135
R6	121	-12	-10	9	9.2	8.9	135 ^b

^aRelease number, sampling duration, cross-shore dye release location x_0 , inner transect integration limit x_{in} , number of downstream transect locations, average number of realizations on each transect $\langle N_j \rangle^{(j)}$ (where $\langle \cdot \rangle^{(j)}$ is the average over all transect locations j), average degrees of freedom on each transect $\langle N_j \rangle^{(j)}$, and the estimated Eulerian decorrelation time τ_{decorr} are shown.

^bFor R3 and R6, data to estimate τ_{decorr} were not available so the largest estimate ($\tau_{decorr} = 135$ s) is used.

surfzone averaged mean alongshore currents (\bar{V}) between 0.07 and 0.37 ms^{-1} , and surfzone averaged \bar{V}_{rot} between 0.036 and 0.090 ms^{-1} (Table 1).

2.2. Dye Release Methods

[16] Concentrated Rhodamine-WT dye (21% by weight) was released continuously at 1.3–7.1 mL s^{-1} into the surfzone during mid- to high tide. The cross-shore dye release location x_0 (in about 1 m depth) varied between -4 and -22 m, with one release (R1) much farther offshore at $x_0 = -54$ m (Table 2). A battery powered peristaltic pump mounted on a 2 m tall heavy metal cart forced dye through a small tube to 0.5 meters above the bed, terminating into a small 10 cm long diffuser hose. Rapid vertical mixing was visually observed, and measured surface dye concentrations were reduced to 400 parts per billion (ppb) within a few meters of the source indicating that concentrated dye (1.2 specific gravity) was quickly diluted to a specific gravity near 1. Although dye was not measured near the bed, dye is expected to be vertically well-mixed due to vigorous surfzone mixing. The possibility of vertically varying dye is discussed in section 6.4.

2.3. Dye Sampling Methods

[17] Dye concentration D was measured with a flow-through fluorometer mounted on a GPS tracked jet ski [Clark *et al.*, 2009], allowing measurements on cross-shore transects through the surfzone where small boats cannot operate. An onboard position display facilitated repetition of predetermined transects. Water was pumped from an intake 20 cm below the surface into a debubbler, thus reducing the number of large bubbles entering the optical instruments. The water subsequently passed through a turbidity sensor to estimate the remaining bubble interference, and finally through a Rhodamine WT fluorometer. Dye fluorescence measurements are corrected for bubble effects [Clark *et al.*, 2009], with resulting root mean square (rms) errors estimated to be less than 2.7% of D . Mixing within the flow-through system smoothes sharp gradients in dye concentration over time scales less than 2.4 s. The time for water to move through the flow-through system and reach the fluorometer varied by ± 0.84 s, resulting in spatial errors (matching dye measurements to GPS positions) of a few meters, dependent upon jet ski speed [Clark *et al.*, 2009].

[18] Dye tracer plumes were sampled for 40 to 121 min durations (Table 2) downstream from the dye source on cross-shore transects (e.g., R3 and R6 examples in Figure 3). The dye plume was allowed to advect past the farthest downstream transect for roughly 20 min prior to sampling, insuring that initial transients had moved beyond the sampling region. Inbound transects were driven from seaward of the dye plume towards the shoreline until the jet ski turned around in roughly 0.5 m water depth (<10 m from the shoreline). Inbound transects were shore normal, uninterrupted, and driven just in front of a broken bore to reduce the number of bubbles entering the flow-through dye sampling system. Outbound transects were not analyzed because large amounts of air was entrained when the jet ski jumped over bores, and transects were often interrupted while avoiding waves. Inbound sampling over the same part of the wave orbital cycle (e.g., just in front of a bore) may bias the cross-shore dye locations by roughly ± 1 –2 m (using linear theory for typical HB06 surfzone conditions). The alongshore distances between transects varied between roughly 20 and 250 m, and the largest downstream distance was 686 m.

[19] Each transect location was repeated 1–4 times before moving to the next location, and the entire pattern was repeated several times. Each transect through the dye plume yields a realization (or snapshot, denoted with an i) of cross-shore dye concentration $D_i(x, y_j)$ at alongshore transect location y_j . The number of transect locations for each release ranged from three (R1) to nine (R6). The number of realizations on a transect is N_j , and the release averaged realizations per transect $\langle N_j \rangle^{(j)}$ (where $\langle \cdot \rangle^{(j)}$ is the average over all transect locations j in a release) varies between 4.5 and 15.3 (Table 2).

[20] Individual $D_i(x, y_j)$ realizations include instrument dye measurement errors (with uncertainty $\pm 0.027 D$) and errors from the ± 0.84 s uncertainty in flow-through system delay time τ [Clark *et al.*, 2009]. The delay time error is assumed to have a Gaussian probability density function (PDF) $P(\tau)$ with 0.84 s standard deviation. Total rms dye measurement errors $\epsilon_i(x, y_j)$ are estimated from squared dye variations and squared dye measurement errors integrated over $P(\tau)$

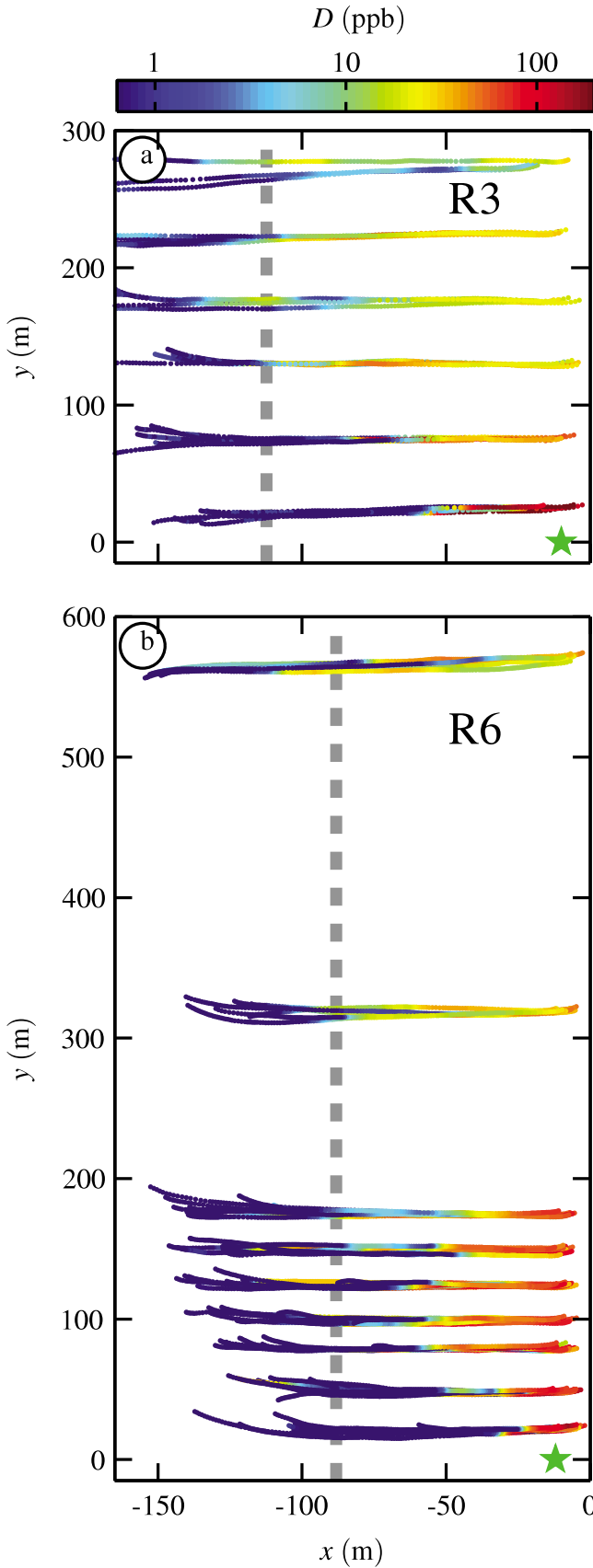
$$\epsilon_i(x, y_j) = \left[\int_{-\infty}^{\infty} [D_i(x - c\tau, y_j) - D_i(x, y_j)]^2 P(\tau) d\tau + \int_{-\infty}^{\infty} [0.027 D_i(x - c\tau, y_j)]^2 P(\tau) d\tau \right]^{1/2}, \quad (2)$$

where c is the roughly 1–5 ms^{-1} jet ski speed. In general, ϵ_i is <20% of D_i .

3. Tracer Means and Moments

3.1. Absolute Averages

[21] Turbulent tracer dispersion has time varying structure, and ensemble averages (over realizations in time) are used to describe mean (or bulk) tracer statistics [e.g., Taylor, 1921; Batchelor, 1949; Csanady, 1973]. Absolute averages are taken in a fixed coordinate frame, and include the effects of both meandering (varying advection of the realization center of mass) and relative diffusion about the realization center of mass. Relative averages remove meandering by averaging in a center of mass coordinate system (relative to



each realization), and isolate the effects of relative diffusion by smaller spatial and temporal scale processes. *Batchelor* [1952], *Csanady* [1973], *Fong and Stacey* [2003], and many others discuss absolute and relative averaging.

[22] For each release, cross-shore profiles of mean (absolute averaged) concentration $\bar{D}(x, y_j)$ at each y_j transect location are constructed by averaging N_j transect realizations $D_i(x, y_j)$ in shoreline coordinates x , i.e.,

$$\bar{D}(x, y_j) = \langle D_i(x, y_j) \rangle^{(i)}, \quad (3)$$

where $\langle \cdot \rangle^{(i)}$ is the average over all realizations i . Absolute averaging is used for simplicity because the interaction of a tracer plume with a boundary (i.e., the beach) complicates the interpretation of relative averages. For example, $D_i(x, y_j)$ realizations with shoreline maxima (shoreline attached), equal dye mass, and different cross-shore widths give varying individual centers of mass at a transect location y_j (Figure 4). The center of mass variation may imply that the plume is meandering, but could also be explained (e.g., this example) by turbulent fluctuations widening some shoreline attached realizations more than others.

[23] Rms errors $\epsilon_{\bar{D}}(x, y_j)$ in the mean $\bar{D}(x, y_j)$ are estimated by

$$\epsilon_{\bar{D}}(x, y_j) = \frac{1}{\sqrt{N_j}} \sqrt{\langle \epsilon_i^2(x, y_j) \rangle^{(i)} + \langle [D_i(x, y_j) - \bar{D}(x, y_j)]^2 \rangle^{(i)}}, \quad (4)$$

where $\langle \epsilon_i^2(x, y_j) \rangle^{(i)}$ is the mean squared dye measurement error, $\langle [D_i(x, y_j) - \bar{D}(x, y_j)]^2 \rangle^{(i)}$ is the dye variance at each x , and N_j is the degrees of freedom at a transect location j (Appendix A). The dye variance is usually much larger than the instrumental error. Using N_j in (4) accounts for consecutive $D_i(x, y_j)$ that are not independent. The N_j are estimated from the Eulerian tracer decorrelation time (Appendix A), where $N_j = 1$ and $N_j = N_j$ correspond to completely dependent and completely independent sampling, respectively (release averaged $\langle N_j \rangle^{(i)}$ are given in Table 2).

3.2. Mean Profile $\bar{D}(x, y_j)$ Cross-Shore Integrated Statistics

[24] Two cross-shore integrated tracer statistics are estimated from mean $\bar{D}(x, y_j)$ profiles; the alongshore tracer transport $M(y_j)$, and the surface-center of mass (first moment) $\mu(y_j)$. These statistics are both functions of y_j , the alongshore distance from the dye source. The jet ski cross-shore transects are driven as shallow as possible without running aground, and the location of the $\bar{D}(x, y_j)$ inner ends vary. To avoid propagating transect end variations into $\bar{D}(x, y_j)$ statistics, the shoreward integral limit is at x_{in} (Table 2), the inner $\bar{D}(x, y_j)$ end that is farthest from the shoreline (for each release). Taking the integral limit at x_{in} biases mean transect statistics equally, rather than randomly as with variable inner ends. The x_{in} are generally shoreward of the cross-shore dye release

Figure 3. Jet ski dye measurements D (concentration in color) during releases (a) R3 and (b) R6 versus cross-shore distance from the shoreline x , and alongshore distance y from the dye source (green star). Only inbound (traveling towards the beach) transects are shown. Dashed gray line indicates the seaward edge of the surfzone.

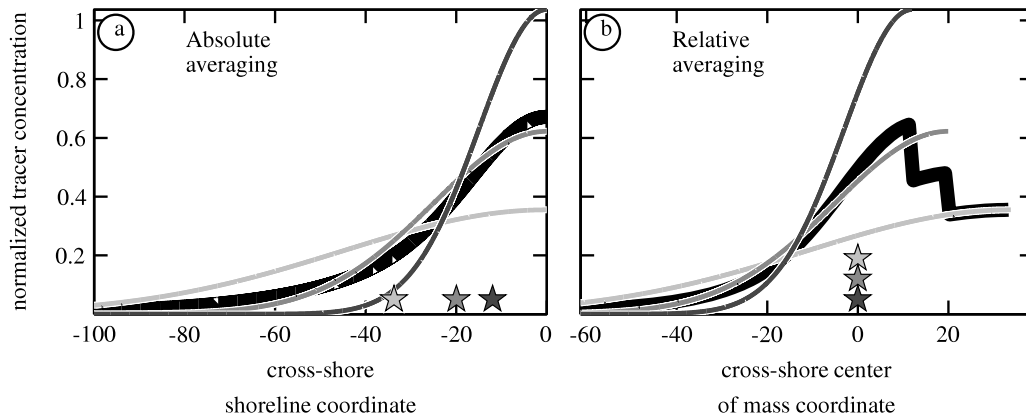


Figure 4. Schematic cross-shore tracer concentration in (a) shoreline and (b) center of mass coordinates, illustrating the difficulty in estimating relative diffusivity near the shoreline (shoreline coordinate zero). Tracer averages (thick black curves) are from three realizations (gray curves) with varying cross-shore widths. The center of mass for each realization is indicated with a star in the corresponding shade of gray.

location x_0 , and little data is discarded. The effect of the unsampled region near the shoreline on $M(y_j)$ is discussed in section 6.4.

[25] An idealized tracer plume conserves alongshore tracer transport (i.e., flux through the xz plane). Assuming vertically well-mixed tracer, alongshore uniform depth $h(x)$ and alongshore current $V(x)$, negligible tracer-alongshore current covariance, and negligible dye offshore of frame 7 (x_{F7}), the mean alongshore tracer transport $M(y_j)$ is defined as

$$M(y_j) = \int_{x_{F7}}^{x_{in}} h(x)V(x)\bar{D}(x, y_j) dx. \quad (5)$$

The transport M at $y = 0$ is given by the estimated pump flow rate ($\text{m}^3 \text{s}^{-1}$) times the initial dye concentration (2.1×10^8 ppb).

[26] The tracer plume surface-center of mass $\mu(y_j)$ is given by the $\bar{D}(x, y_j)$ first moment

$$\mu(y_j) = \frac{\int_{x_{out}}^{x_{in}} x\bar{D}(x, y_j) dx}{\int_{x_{out}}^{x_{in}} \bar{D}(x, y_j) dx}, \quad (6)$$

where the offshore limit of $\bar{D}(x, y_j)$, x_{out} , is always seaward of the tracer plume. For non-shoreline attached tracer plumes (i.e., no plume-shoreline interaction) and no cross-shore advection, $\mu(y_j)$ is expected to remain constant [e.g., *Csanady, 1973*]. In contrast, shoreline attached plumes spread (i.e., disperse) away from the shoreline, and $\mu(y_j)$ magnitudes are expected to increase downstream. Similar to $\mu(y_j)$, the shoreline also complicates estimates of the plume second moment, as discussed in section 5.

[27] Errors $\epsilon_M(y_j)$ and $\epsilon_\mu(y_j)$ in cross-shore tracer statistics $M(y_j)$ and $\mu(y_j)$ are estimated using Monte Carlo simulations. For each transect, 10^4 simulated $\bar{D}(x, y_j)$ are generated from the observed $\bar{D}(x, y_j)$ plus Gaussian noise, where the noise variance is equal to $\epsilon_{\bar{D}}^2(x, y_j)$ (4). The tracer statistic errors $\epsilon_M(y_j)$ and $\epsilon_\mu(y_j)$ are estimated as the standard deviation of simulated $M(y_j)$ and $\mu(y_j)$ calculated from the simulated $\bar{D}(x, y_j)$. The errors are dependent on the $\epsilon_{\bar{D}}^2$ decorrelation

length-scale, thus the Monte Carlo process is repeated with cross-shore decorrelation length-scales between zero and twice the surfzone width L_x . The maximum $\epsilon_M(y_j)$ and $\epsilon_\mu(y_j)$ over the range of decorrelation length-scales, are used.

4. Observations of Surfzone Tracer Plumes

4.1. Tracer Cross-Shore Structure

[28] Continuous surfzone dye releases in an alongshore current form tracer plumes (e.g., Figure 3) similar to a smokestack plume in the wind, with plume axis parallel to the shoreline. The positive alongshore current (Figure 2b) advects dye downstream ($+y$) from the dye source (green star, Figure 3). The initially concentrated dye dilutes and spreads cross-shore as it is advected downstream. The plumes were visually patchy with adjacent high and low concentration areas at all alongshore distances from the dye source, and the patch length-scale increased with distance. Bores did not “surf” dye to the shoreline, although the plume cross-shore width visually widened with each passing bore [e.g., *Feddersen, 2007*]. Bore-mixing was most apparent when plume widths were <10 m, and difficult to observe when plume widths were visually >40 m.

[29] At all cross-shore locations, individual $D_i(x, y_j)$ vary about the mean (e.g., Figure 5). At transect locations close to the source (e.g., Figures 5a and 5d), dye maxima are sometimes seaward of the shoreline, and have “meandering like” variations (roughly ± 10 m). Farther downstream from the dye source (Figures 5b, 5c, 5e, and 5f) the $D_i(x, y_j)$ realizations are more shoreline attached, and may significantly interact with the shoreline boundary.

[30] The mean tracer profile errors $\epsilon_{\bar{D}}(x, y_j)$ (4), indicated by the light-colored regions about the mean in Figure 6, combine variability between realizations (e.g., Figure 5) and dye measurement errors (2). For all realizations, dye inter-realization variance (last term of (4)) dominates $\epsilon_{\bar{D}}(x, y_j)$ and is on average 45 times greater than mean squared dye measurement errors. The $\epsilon_{\bar{D}}(x, y_j)$ increase with increasing $\bar{D}(x, y_j)$ (e.g., Figure 6). The R3 $\epsilon_{\bar{D}}(x, y_j)$ are larger than R6 because (in addition to larger $\bar{D}(x, y_j)$) R3 has shorter

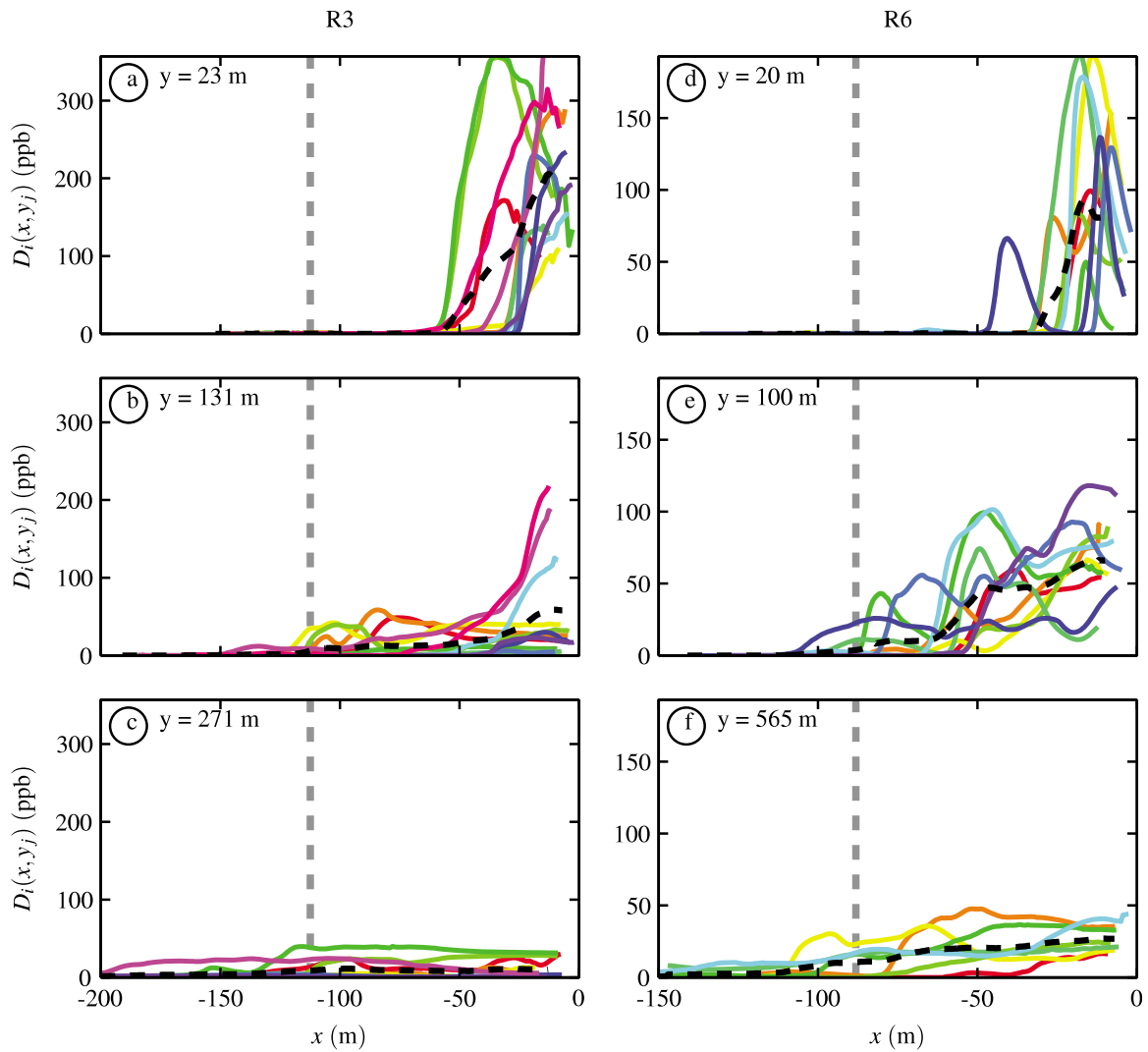


Figure 5. Cross-shore dye concentration transects $D_i(x, y_j)$ versus x for (a–c) R3 and (d–f) R6 at three downstream locations y from the dye source (see top left). Individual realizations $D_i(x, y_j)$ are in color and the mean \bar{D} is a dashed black curve. R3 (Figures 5a–5c) and R6 (Figures 5d–5f) have different vertical scales.

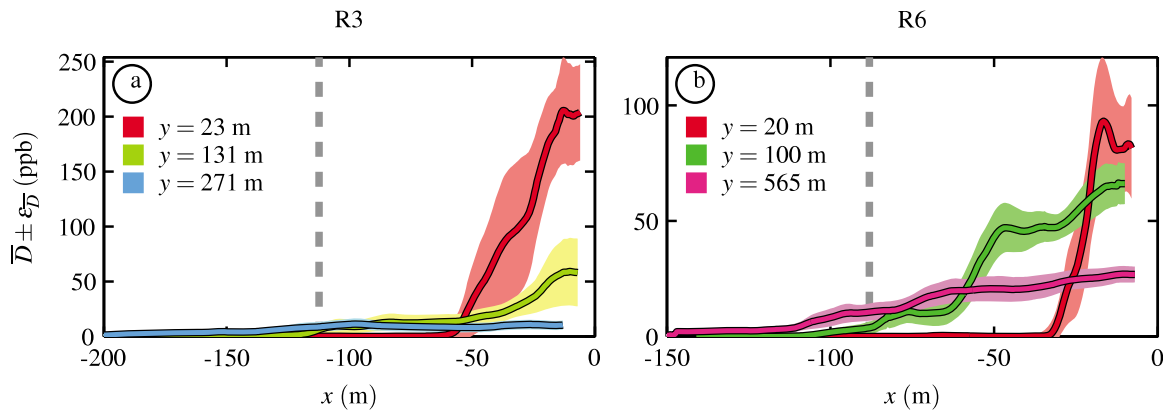


Figure 6. Mean dye profile curves $\bar{D}(x, y_j)$ with lighter regions indicating $\bar{D}(x, y_j) \pm \epsilon_{\bar{D}}(x, y_j)$, for dye releases (a) R3 and (b) R6 at three alongshore distances y from the dye source (see legend). The dashed gray line indicates the seaward edge of the surfzone. Vertical scales differ.

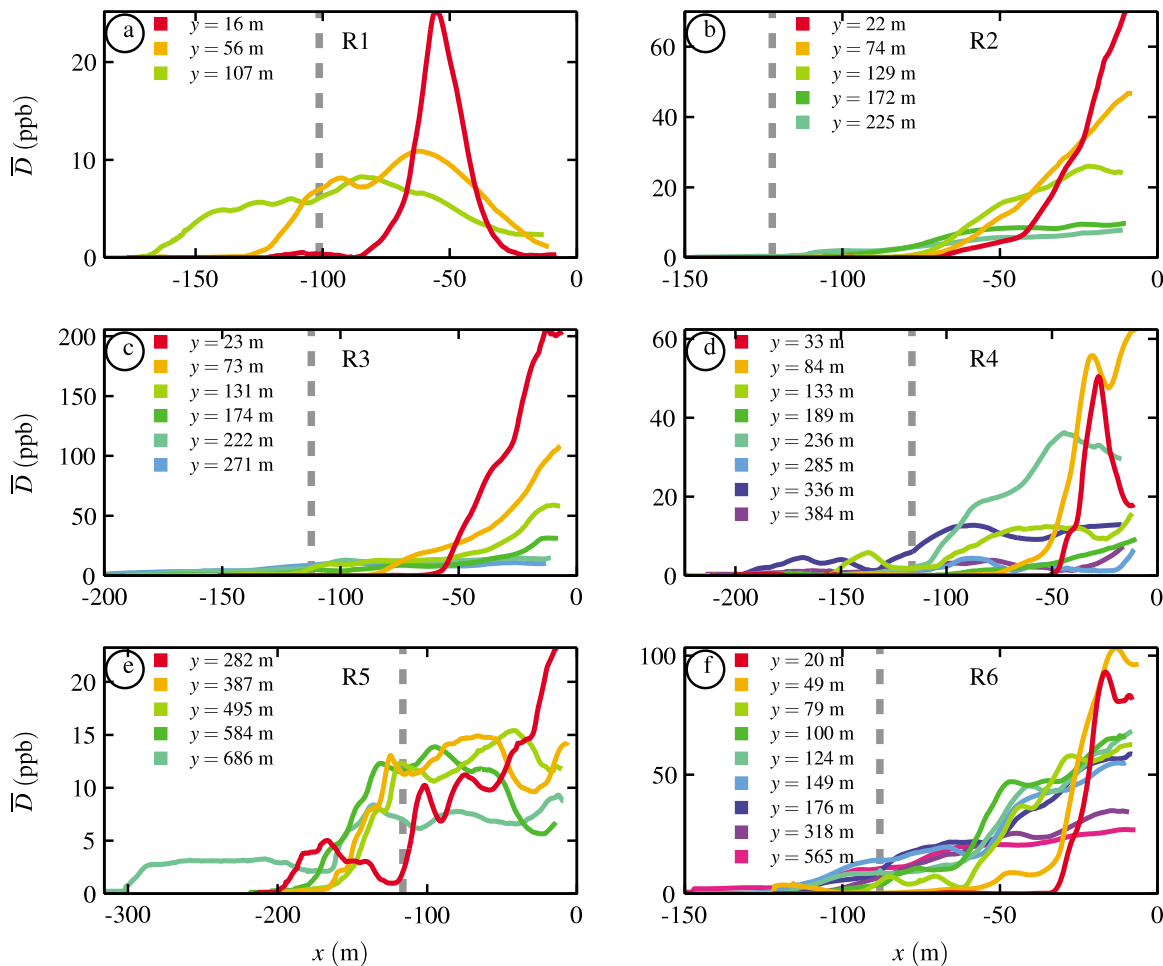


Figure 7. Mean tracer concentration $\bar{D}(x, y_j)$ versus x for releases (a) R1, (b) R2, (c) R3, (d) R4, (e) R5, and (f) R6. Colors indicate different downstream alongshore distances y (see legends). The surfzone is between $x = 0$ m and the vertical dashed gray line. Mean (over all releases) fractional errors $\epsilon_{\bar{D}}(x, y_j)/\bar{D}(x, y_j)$ are 0.38 ± 0.16 (for $D > 5$ ppb), and 0.78 ± 0.29 (for $D < 5$ ppb). Vertical and horizontal scales vary.

times between transects, resulting in lower degrees-of-freedom \mathcal{N}_j (Table 2).

[31] The mean tracer profiles $\bar{D}(x, y_j)$ (Figure 7) average over stirring and meandering, and are smoother than individual profiles $D_i(x, y_j)$ (e.g., Figure 5). Most mean profiles $\bar{D}(x, y_j)$ are shoreline attached with maxima at or near the shoreline (Figure 7). The exception, R1, has maxima in the mid- to outer-surfzone, likely because dye was released in the mid- to outer-surfzone ($x_0 = -54$ m), and y_j sampling distances are short (Figure 7a). On all releases except R5, the initially narrow $\bar{D}(x, y_j)$ profiles disperse across the surfzone and peak concentrations decrease with downstream distance from the source (Figure 7). Release R5 was sampled far downstream of the dye source ($y_j > 282$ m) where tracer had already spread (i.e., saturated) across the surfzone (Figure 7e), with smaller concentrations seaward of the surfzone. The two farthest downstream $\bar{D}(x, y_j)$ profiles of R3 (Figure 7c, with expanded scale in Figure 8) and R6 (Figure 7f) are also surfzone saturated. The strong gradients in \bar{D} profiles seaward of the saturated surfzone are consistent with decreased diffusivity.

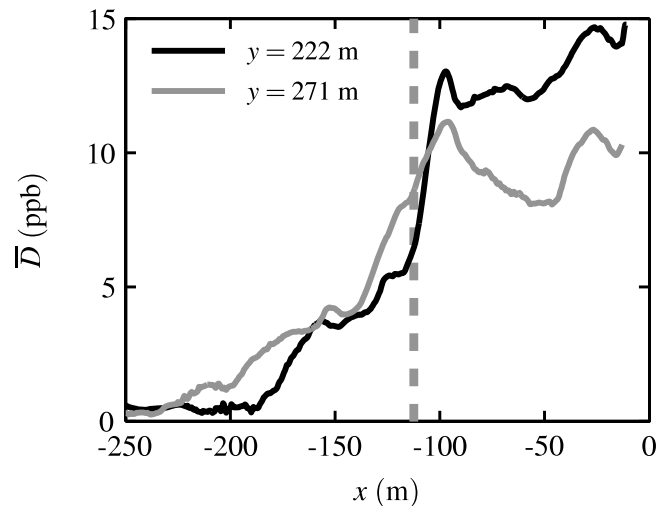


Figure 8. $\bar{D}(x, y_j)$ versus x for the two R3 transects farthest downstream from the dye source (expanded view of Figure 7c). The surfzone is between $x = 0$ m and the vertical dashed gray line.

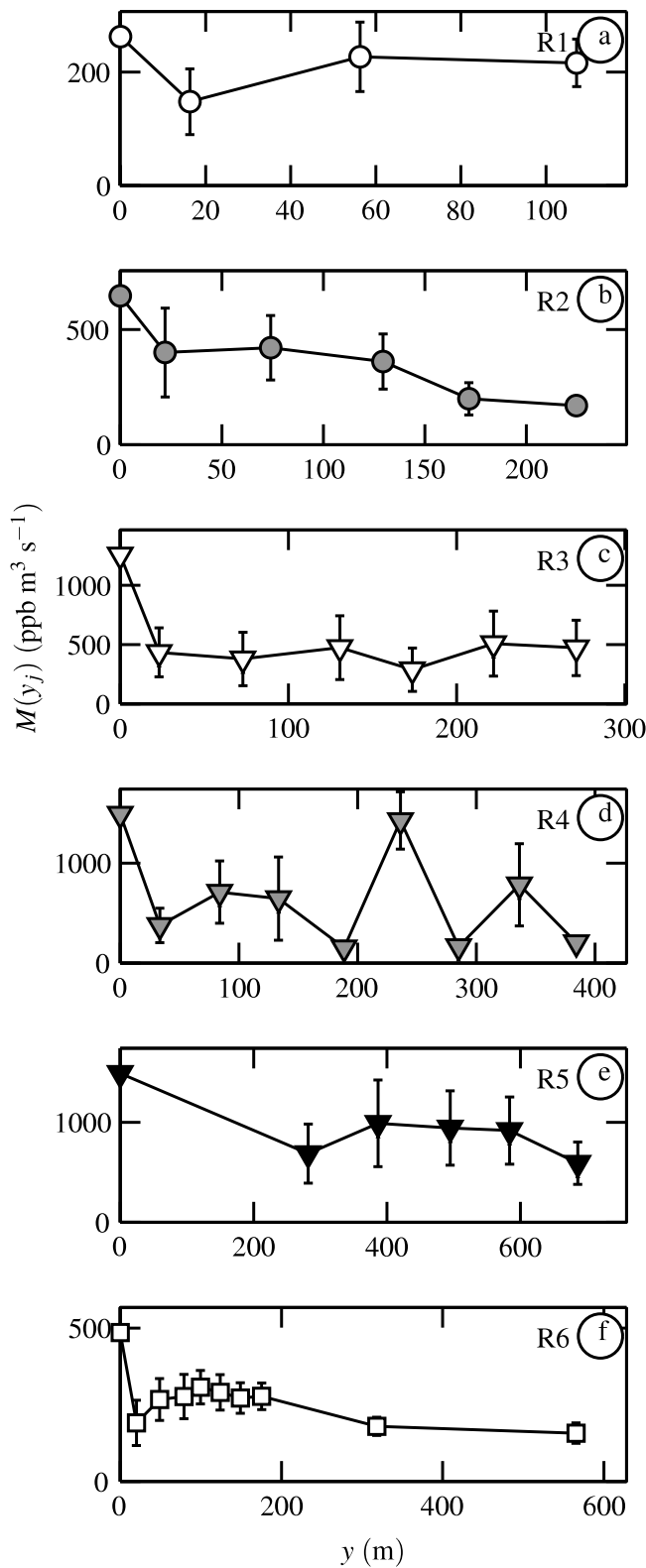


Figure 9. Tracer alongshore transport $M(y_j)$ (5) versus y , with error bars $\pm\epsilon_M$ for releases (a) R1, (b) R2, (c) R3, (d) R4, (e) R5, and (f) R6. The initial condition at $y = 0$ m is the injected dye transport (concentration times flow-rate).

4.2. Alongshore Evolution of $\bar{D}(x, y_j)$ Statistics

[32] The downstream y evolutions of tracer transport $M(y_j)$ (5) and surface-center of mass $\mu(y_j)$ (6), estimated using $\bar{D}(x, y_j)$ mean profiles, are examined. Tracer seaward of frame 7 ($x < -150$ m from the MSL shoreline) is neglected (5) and reduces some $M(y_j)$ at large y . Alongshore variation in $V(x)$ is also neglected, and complete vertical mixing is assumed. Nevertheless, for all releases, the downstream (i.e., not including $y = 0$ m) tracer transports $M(y > 0$ m) generally vary by less than a factor of 2 (Figure 9), and (except for R4) are either roughly constant downstream (e.g., R1 and R3) or monotonically decrease (e.g., R2). Thus, a significant amount of the dye measured on the first transect ($y_j > 0$ m) is accounted for farther downstream.

[33] The reason that the pump-rate calculated $M(y = 0$ m) are larger than downstream estimated $M(y > 0$ m) is not known. Consistent fluorometer calibrations over multiple batches of calibration standards indicate that fluorometer instrumentation error is not the cause. Other possible reasons are discussed in section 6.4. All other tracer moments considered here (e.g., μ (6)) are normalized by the cross-shore surface tracer integral on each transect, thus reducing the effect of tracer transport variations.

[34] The $\bar{D}(x, y_j)$ (Figure 7) tracer surface-centers of mass $\mu(y_j)$ (6) are initially grouped (Figure 10) near the cross-shore dye release locations x_0 (Table 2). Farther downstream, the shoreline attached R2–R6 $\mu(y_j)$ generally move seaward, consistent with shoreline attached dye profiles (Figures 7b–7f) broadened by cross-shore dispersion (Figure 10, and section 5.3), and does not likely represent cross-shore advection of the mean plume. In contrast, R1 tracer was released mid-surfzone (Table 2) and the $\mu(y_j)$ appear (Figure 7a) to move seaward by advection of the mean plume, and not plume widening near a boundary. For

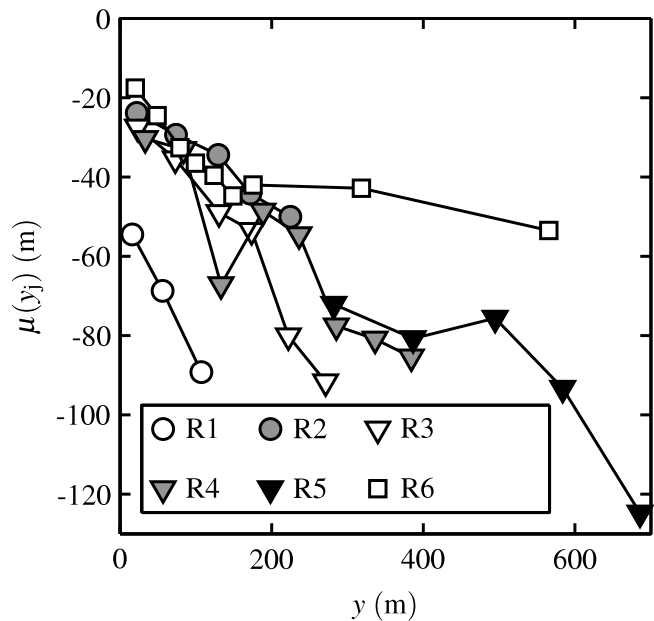


Figure 10. Tracer surface-center of mass $\mu(y_j)$ (6) versus y . The mean $\mu(y_j)$ error over all transects and releases is $\epsilon_\mu(y_j) \approx 14$ m.

shoreline attached profiles, surfzone saturation and a lower diffusivity seaward of the surfzone would result in decreased seaward $\mu(y_j)$ movement at large y , and is apparent in release R6.

5. Dispersive Plume Widening and Surfzone Cross-Shore Diffusivity κ_{xx}

5.1. Simple Diffusion Models

[35] Surfzone cross-shore turbulent mixing results from many mechanisms with different time- and length-scales. The appropriate model diffusivity depends on the model dynamics and the scales resolved. For example, a two-dimensional (2D) horizontal eddy-resolving Boussinesq model [e.g., *Johnson and Pattiaratchi, 2006; Spydel and Feddersen, 2009*] would require a much smaller diffusivity than a simple bulk model averaged over longer time scales that combine eddy stirring into a bulk (Fickian) diffusivity. Here, a simple Fickian diffusion model is presented that provides an analytic method for estimating the bulk diffusivity from observations of $\bar{D}(x, y_j)$, and also has solutions relating diffusivity, tracer surface-center of mass, and dilution of maximum tracer concentration.

[36] The time invariant 2-D Fickian advection-diffusion model for vertically-mixed mean tracer concentrations $\bar{D}(x, y)$ with a tracer source Q_0 ($\text{m}^3 \text{ ppb s}^{-1}$) at $x = x_0$ and $y = 0$, and assuming a constant cross-shore diffusivity κ_{xx} (Brownian diffusion regime), a long narrow plume ($\partial^2/\partial y^2 \ll \partial^2/\partial x^2$), and cross-shore variable depth $h(x)$ is

$$h(x)V(x) \frac{\partial \bar{D}(x, y)}{\partial y} = \kappa_{xx} \frac{\partial}{\partial x} \left(h(x) \frac{\partial \bar{D}(x, y)}{\partial x} \right) + Q_0 \delta(x - x_0, y). \quad (7)$$

[37] Assuming constant surfzone averaged depth \bar{h} (neglecting dh/dx) and that tracer is advected downstream by the surfzone averaged mean alongshore current \bar{V} , (7) becomes

$$\bar{V} \frac{\partial \bar{D}(x, y)}{\partial y} = \kappa_{xx} \frac{\partial^2 \bar{D}(x, y)}{\partial x^2} + \frac{Q_0}{\bar{h}} \delta(x - x_0, y) \quad (8)$$

and allows for analytic solutions. For HB06 cross-shore variable bathymetry $h(x)$ (Figure 1b), observed $V(x)$ (Figure 2b), and dye release locations (Table 2), numerical solutions to the constant (8) and cross-shore varying depth and alongshore current (7) equations are similar (particularly for $y > 50$ m), as is the evolution of cross-shore integrated moments. One reason for the similar solutions may be the relatively flat terraced surfzone bathymetry (see $-75 < X < -10$ m in Figure 1b). Defining a plume alongshore advection time t_p

$$t_p = \bar{V}^{-1} y,$$

where t_p is the time for a section of the plume moving with \bar{V} to reach a downstream location y , (8) reduces to the familiar 1-D diffusion equation

$$\frac{\partial \bar{D}(x, t_p)}{\partial t_p} = \kappa_{xx} \frac{\partial^2 \bar{D}(x, t_p)}{\partial x^2} + \hat{Q}_0 \delta(x - x_0, t_p), \quad (9)$$

where $\hat{Q}_0 = Q_0/(\bar{h}\bar{V})$. On an unbounded domain (9) has a Gaussian solution

$$\bar{D}(x, t_p) = \frac{\hat{Q}_0}{\sqrt{4\pi\kappa_{xx}t_p}} \exp\left[-\frac{(x-x_0)^2}{4\kappa_{xx}t_p}\right], \quad (10)$$

where κ_{xx} is related to the tracer second moment σ^2 [e.g., *Csanady, 1973*]

$$\kappa_{xx} = \frac{1}{2} \frac{d\sigma^2}{dt_p} \quad (11)$$

and σ^2 is defined as

$$\sigma^2 = \frac{\int_{-\infty}^{\infty} [x - \mu]^2 \bar{D}(x, y_j) dx}{\int_{-\infty}^{\infty} \bar{D}(x, y_j) dx}, \quad (12)$$

where μ (6) is calculated over the $\pm\infty$ domain. On a semi-infinite domain ($-\infty < x < 0$) with a no-flux boundary condition at the $x = 0$ shoreline

$$\left. \frac{\partial \bar{D}}{\partial x} \right|_{x=0} = 0,$$

(9) has the method of images solution

$$\bar{D}(x, t_p) = \frac{\hat{Q}_0}{\sqrt{4\pi\kappa_{xx}t_p}} \left[\exp\left(-\frac{(x-x_0)^2}{4\kappa_{xx}t_p}\right) + \exp\left(-\frac{(x+x_0)^2}{4\kappa_{xx}t_p}\right) \right]. \quad (13)$$

[38] For the case of dye released at the shoreline ($x_0 = 0$), the solution (13) is a shoreline attached half-Gaussian. The cross-shore diffusivity for (13) is

$$\kappa_{xx} = \frac{1}{2} \frac{d\sigma_{sl}^2}{dt_p}, \quad (14)$$

where σ_{sl}^2 is the shoreline based second moment

$$\sigma_{sl}^2 = \frac{\int_{-\infty}^0 x^2 \bar{D} dx}{\int_{-\infty}^0 \bar{D} dx}. \quad (15)$$

[39] Thus, for shoreline attached plumes (R2, R3, R4, and R6) κ_{xx} is estimated from (14) and (15), with modification (section 5.2). For plumes that are well separated from the shoreline (i.e., R1), κ_{xx} is estimated from (11) and (12). Applying (14) and (15) to numerical solutions of the full advection diffusion equation (7) with observed release parameters (Table 2), and cross-shore varying $h(x)$ (Figure 1) and $V(x)$ (Figure 2b), yields κ_{xx} estimates within 10% of the modeled value. Therefore, the cross-shore uniform h and \bar{V} approximations are not expected to bias κ_{xx} significantly.

5.2. Estimating Surfzone κ_{xx}

[40] Surfzone absolute κ_{xx} are estimated by applying (14) and (15) to shoreline attached mean tracer profiles $\bar{D}(x, y_j)$, with some adjustments to capture surfzone specific κ_{xx} . Because σ_{sl}^2 is sensitive to tracer seaward of the surfzone, a

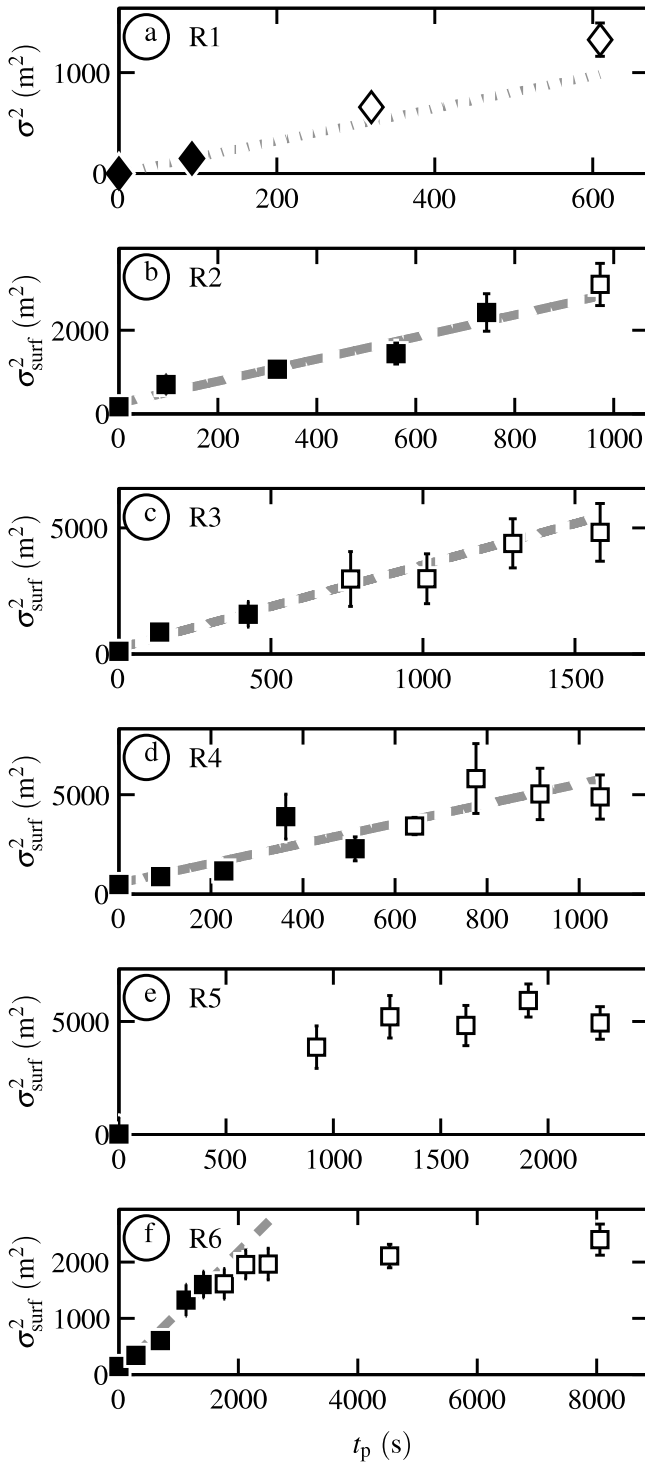


Figure 11. Plot of $\sigma^2 \pm \epsilon_{\sigma^2}$ (Figure 11a) and $\sigma_{\text{surf}}^2 \pm \epsilon_{\sigma_{\text{surf}}^2}$ (Figures 11b–11f) versus T_p for releases (a) R1, (b) R2, (c) R3, (d) R4, (e) R5, and (f) R6. Black symbols indicate points used in the κ_{xx} fits (dashed gray curves) between $T_p = 0$ and the farthest downstream transect with dye largely confined within the surfzone ($\mathcal{R} \leq \mathcal{R}_0$). Errors ϵ_{σ^2} and $\epsilon_{\sigma_{\text{surf}}^2}$ are estimated in the same manner as ϵ_M and ϵ_μ (section 3.2).

surfzone-specific 2nd moment σ_{surf}^2 is defined, similar to σ_{sl}^2 , but integrated only over the surfzone, i.e.,

$$\sigma_{\text{surf}}^2(y_j) = \frac{\int_{-L_x}^{x_{\text{in}}} \overline{D}(x, y_j) x^2 dx}{\int_{-L_x}^{x_{\text{in}}} \overline{D}(x, y_j) dx}, \quad (16)$$

thus excluding dye seaward of the surfzone. With a delta function source at $x = x_0$ (Table 2) and $y = 0$ (i.e., $T_p = 0$), $\sigma_{\text{surf}}^2(0) = x_0^2$.

[41] With a reduced κ_{xx} seaward of the surfzone [e.g., *Harris et al.*, 1963], initially rapid surfzone cross-shore dispersion would slow as a tracer spreads offshore. A surfzone saturation ratio \mathcal{R} is used to select transects with dye well contained in the surfzone, and exclude surfzone saturated transects effected by reduced seaward κ_{xx} . For each transect, \mathcal{R} is the ratio of the measured $\sigma_{\text{surf}}^2(y_j)$ to that of a saturated surfzone (i.e., constant surfzone concentration)

$$\mathcal{R} = \sigma_{\text{surf}}^2(y_j) / \left[\frac{\int_{-L_x}^{x_{\text{in}}} x^2 dx}{\int_{-L_x}^{x_{\text{in}}} dx} \right]. \quad (17)$$

Unsaturated transects, between the source and the farthest downstream transect satisfying a surfzone saturation ratio criterion $\mathcal{R} < \mathcal{R}_0$, are included in κ_{xx} estimates. The cutoff threshold $\mathcal{R}_0 = 0.55$ is chosen to include many $\sigma_{\text{surf}}^2(y_j)$ in κ_{xx} fits while not biasing κ_{xx} estimates by more than 10% (Appendix B).

[42] For shoreline attached releases (R2, R3, R4, R6), surfzone κ_{xx} is estimated from least squares σ_{surf}^2 versus T_p fits, i.e.,

$$\sigma_{\text{surf}}^2 = 2\kappa_{xx}T_p + \beta, \quad (18)$$

where κ_{xx} and β are fit constants, and from (15) β is expected to be close to the initial condition x_0^2 . The κ_{xx} error ϵ_κ is estimated from the fit slope error assuming the variance of the residuals is equal to $\epsilon_{\sigma_{\text{surf}}^2}$ [e.g., *Wunsch*, 1996], where $\epsilon_{\sigma_{\text{surf}}^2}$ is estimated with the same Monte Carlo methods as ϵ_M and ϵ_μ (section 3.2). All transects between the release location and the farthest downstream transect with $\mathcal{R} \leq \mathcal{R}_0 = 0.55$ are included in the fit (solid black symbols, Figures 11b, 11c, 11d, and 11f). For shoreline attached releases, estimated $\kappa_{xx} \pm \epsilon_\kappa$ range from 0.5 ± 0.08 to 2.5 ± 0.62 $\text{m}^2 \text{s}^{-1}$ with generally high squared correlation coefficients r^2 (Table 3). The R5 κ_{xx} is not estimated because all downstream transects are surfzone saturated, with $\mathcal{R} > 0.55$ (Figure 11e).

[43] For release R1 with mid-surfzone release location, mean tracer profiles $\overline{D}(x, y_j)$ (Figure 7a) are not shoreline attached, thus (14) through (17) do not apply. The non-shoreline attached R1 surfzone κ_{xx} is estimated using the common definition (11) for absolute dispersion without a boundary [e.g., *Fong and Stacey*, 2003; *Jones et al.*, 2008], where the cross-shore moments μ and σ^2 are integrated from x_{in} to the seaward transect limit x_{out} . Using the initial condition $\sigma^2 = 0$ (at $T_p = 0$) and the first downstream σ^2 (surfzone contained by inspection, Figure 7), the resulting best-fit is $\kappa_{xx} = 0.8 \pm 0.31$ $\text{m}^2 \text{s}^{-1}$, and r^2 cannot be estimated from the two point fit.

Table 3. Estimated κ_{xx} Fits^a

	$2[\kappa_{xx} \pm \epsilon_{\kappa}]t_p + \beta$	r^2
R1	$2[0.8 \pm 0.31]t_p + 0$	-
R2	$2[1.3 \pm 0.26]t_p + 251$	0.94
R3	$2[1.6 \pm 0.68]t_p + 233$	0.95
R4	$2[2.5 \pm 0.62]t_p + 545$	0.56
R6	$2[0.5 \pm 0.08]t_p + 51$	0.97

^aEstimated κ_{xx} from a nonshoreline attached σ^2 versus t_p fit (R1) and shoreline attached σ_{surf}^2 versus t_p fits (R2, R3, R4, and R6). Squared correlations r^2 are given for all releases, with an exception for R1 where a two point fit gives the trivial result $r^2 = 1$.

5.3. Half-Gaussian Shoreline-Attached Model Data Comparison

[44] For shoreline attached R2, R3, R4, and R6 releases, the observed downstream evolution of \bar{D} is similar to the half-Gaussian solution (13) with $x_0 = 0$ m. For example, within the surfzone the observed σ_{surf}^2 increase linearly with t_p (black symbols in Figures 11b, 11c, 11d, and 11f) with generally high r^2 (Table 3) as is expected for (13) and (14), and is consistent with assumption (section 5.1) of constant (in time and space) surfzone κ_{xx} . This model also predicts the downstream evolution of the maximum tracer $\bar{D}_{\text{max}}^{(p)}$

$$\bar{D}_{\text{max}}^{(p)} = \frac{2\hat{Q}_0}{(4\pi\kappa_{xx}t_p)^{1/2}} \quad (19)$$

and surface-center of mass $\mu^{(p)}$

$$\mu^{(p)} = \frac{\int_{-\infty}^0 xG(x_0=0)dx}{\int_{-\infty}^0 G(x_0=0)dx} = -2(\kappa_{xx}t_p/\pi)^{1/2}, \quad (20)$$

where $G(x_0 = 0)$ is the shoreline-attached half-Gaussian solution (13) with dye released at $x_0 = 0$. Note that $\mu^{(p)}$ moves offshore owing to the presence of the shoreline, not from advection. Both predictions are now compared with observations using the estimated surfzone κ_{xx} .

[45] For the R2, R3, R4, and R6 transects used in κ_{xx} estimation (solid symbols in Figure 11b, 11c, 11d, and 11f), and representative of surfzone mixing, the observed \bar{D}_{max} and predicted $\bar{D}_{\text{max}}^{(p)}$ (19) are consistent (Figure 12a). The predictions are slightly larger than the observations, and may result from using pump rate estimated $\hat{Q}_0 = M(y = 0 \text{ m})$ (larger than transect estimates, Figure 9) in \hat{Q}_0 (19) or higher tracer concentrations near the shoreline ($x > x_{\text{in}}$, Table 2) where the jet ski does not sample. Although the R3 and R6 $\bar{D}_{\text{max}}^{(p)}$ have large errors at the first downstream transect, the skill (defined as $1 - \langle (\bar{D}_{\text{max}}^{(p)} - \bar{D}_{\text{max}})^2 \rangle / \langle \bar{D}_{\text{max}}^2 \rangle$ over all releases) of 0.76 is high. The observed μ and predicted $\mu^{(p)}$ are also consistent (Figure 12b) with skill (defined similarly to \bar{D}_{max} skill) of 0.90. The shoreward bias of $\mu^{(p)}$ relative to μ (Figure 12b), may result from assuming a shoreline release ($x_0 = 0$ in (20)) in $\mu^{(p)}$. In addition μ estimates may be biased seaward by neglecting the near-shoreline region between x_{in} (Table 2) and the $x = 0$ m shoreline, where the jet ski does not sample. The seaward $\mu(y_j)$ movement for R2–R6 can be explained as dispersive widening of the shoreline attached plume near a boundary (e.g., Figures 7b–7f). The linear σ_{surf}^2 growth with t_p , the predicted decrease in normalized maxima, and the correspondence of μ and $\mu^{(p)}$, all indicate

(13) well describes the downstream evolution of surfzone contained tracer released near the shoreline.

[46] The shoreline attached moment $\sigma_{\text{surf}}^2(y_j)$ (16) and the half-Gaussian solution (13) assume that the \bar{D}_{max} cross-shore locations remain at the shoreline, however the observed locations vary slightly (Figure 7). Consistent with the assumed shoreline maxima, the ‘‘Péclet numbers’’ (LU/κ_{xx}) for shoreline attached releases are small (< 0.12), where U is the mean cross-shore velocity of the tracer maxima (for profiles used in κ_{xx} fits), $L = Ut_{\text{max}}$, and t_{max} is the maximum t_p included in κ_{xx} fits. The small ‘‘Péclet numbers’’ and the agreement between μ and $\mu^{(p)}$ are consistent with neglecting cross-shore advection for shoreline attached profiles. In contrast, the ‘‘Péclet number’’ for the non-shoreline attached

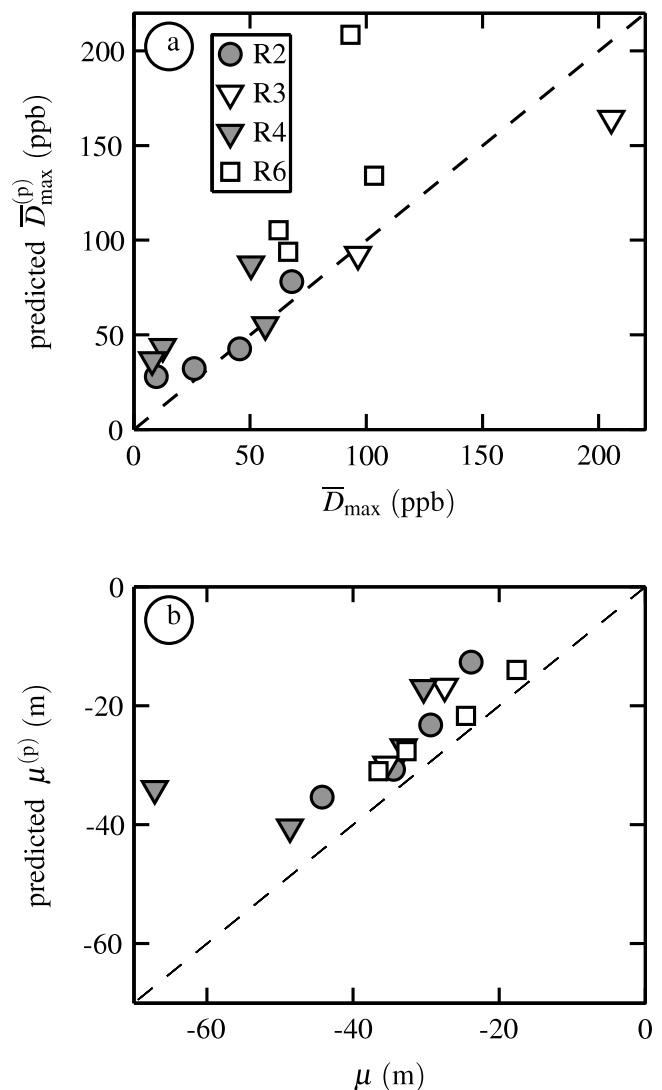


Figure 12. (a) Predicted tracer maxima $\bar{D}_{\text{max}}^{(p)}$ versus observed \bar{D}_{max} , and (b) predicted $\mu^{(p)}$ versus observed μ , for surfzone-contained shoreline attached profiles used in κ_{xx} fits (releases R2, R3, R4, and R6). The predicted $\bar{D}_{\text{max}}^{(p)} = 2\hat{Q}_0/(4\pi\kappa_{xx}t_p)^{1/2}$ (19) and $\mu^{(p)} = -2\sqrt{\kappa_{xx}t_p/\pi}$ (20) use the observed best-fit κ_{xx} (Figures 11b, 11c, 11d, and 11f). The dashed line indicates perfect agreement. The skill in Figure 12a is 0.76, and the skill in Figure 12b is 0.90.

R1 is 3.9 and the cross-shore advection is accounted for in (11) and (12).

6. Discussion

6.1. Surfzone κ_{xx} Comparisons

[47] Previous surfzone field experiments have used the alongshore distribution of point-released dye at the shoreline to estimate κ_{yy} , but lack the cross-shore tracer measurements required to estimate κ_{xx} quantitatively. Detailed surfzone tracer κ_{xx} comparisons are therefore not possible, but the κ_{xx} estimated here (Table 3) are within the range of previous κ values [Inman *et al.*, 1971; Clarke *et al.*, 2007]. GPS-tracked drifters, designed to duck under breaking waves and avoid surfing onshore, have been used to estimate surfzone cross-shore diffusivities $\kappa_{xx}^{(d)}$ with alongshore uniform [Spydell *et al.*, 2007, 2009] and rip channel [e.g., Johnson and Pattiaratchi, 2004; Brown *et al.*, 2009] bathymetries. During the HB06 experiment, drifter-based surfzone $\kappa_{xx}^{(d)}$ were estimated [Spydell *et al.*, 2009], but on different days than dye. Observed dye and asymptotic (long-time) drifter κ_{xx} have similar magnitudes (around $1 \text{ m}^2 \text{ s}^{-1}$).

[48] The HB06 drifter-derived $\kappa_{xx}^{(d)}$ were time-dependent. At times less than the drifter Lagrangian time-scale T_{xx} of $O(100 \text{ s})$, the drifter $\kappa_{xx}^{(d)}$ increase quasi-ballistically ($\sigma^2 \sim t^2$ or $\kappa_{xx} \sim t$) towards a peak value [Spydell *et al.*, 2009]. In contrast, tracer-derived surfzone κ_{xx} are roughly constant in time and $\sigma_{\text{surf}}^2 \sim t$ (Figure 11), indicating Brownian diffusion. However the first dye transects occur near $T_p = 100 \text{ s}$ where the drifter ballistic regime generally ends [Spydell *et al.*, 2009], and unobserved ballistic tracer dispersion may have occurred between the first transects and the dye source (where $T_p \lesssim T_{xx}$).

[49] For $t > T_{xx}$, drifter $\kappa_{xx}^{(d)}$ gradually decreased [Spydell *et al.*, 2009], possibly because drifters sampled the lower diffusivity seaward of the surfzone. Recent dye dispersion studies seaward of the surfzone in $\sim 10 \text{ m}$ water depth [Fong and Stacey, 2003; Jones *et al.*, 2008], with similar plume widths to those observed here, found absolute diffusivities roughly 10 times smaller than the surfzone κ_{xx} here. Note that σ_{surf}^2 is surfzone integrated, and therefore not an appropriate variable to examine seaward κ_{xx} .

6.2. Surfzone Saturation and Diffusion Seaward of the Surfzone

[50] The $\bar{D}(x, y_j)$ profiles far-downstream (largest y) have roughly constant magnitude (i.e., are saturated) across the surfzone for releases R3, R5, and R6 (Figures 7c, 7e, and 7f), and the far-downstream R3 and R5 transects have sharp $\bar{D}(x, y_j)$ gradients at the seaward edge of the surfzone (e.g., Figures 7e and 8). These $\bar{D}(x, y_j)$ profiles are consistent with a larger surfzone κ_{xx} smoothing dye gradients inside the surfzone and a smaller κ_{xx} slowly mixing dye farther seaward. In contrast, the two farthest downstream R1 transects have significant amounts of dye outside the surfzone (Figure 7a), but the dye plume continues to spread. The continued dispersion seaward of the surfzone may result from absolute averages over meandering of the non-shoreline attached plume, but could also result from rip currents that transport dye well beyond the seaward edge of the surfzone.

[51] Although σ_{surf}^2 excludes data (and dispersion) seaward of the surfzone, constant σ_{surf} versus T_p does indicate

surfzone saturation. The $\sigma_{\text{surf}}(y_j)$ for R6 initially grow inside the surfzone, but become constant for $T_p > 2000 \text{ s}$ in agreement with saturated profiles (Figure 7f). In addition, the nearly constant σ_{surf} in the farthest downstream transects of R4 (Figure 11d) suggest surfzone saturation that is not visually apparent in the $\bar{D}(x, y_j)$ profiles (Figure 7d).

6.3. Parameterizing κ_{xx}

[52] Previous dye dispersion studies [e.g., Harris *et al.*, 1963; Inman *et al.*, 1971] parameterized diffusivity with

$$\kappa_{xx} \sim \frac{H_b^2}{T} \quad (21)$$

or

$$\kappa_{xx} \sim \frac{H_b L_x}{T}, \quad (22)$$

where H_b is the wave height at the breakpoint, and T is a wave period. With planar bathymetry and constant $\gamma = H/h$, these two parameterizations (21, 22) are essentially equivalent. Although previous work found agreement between surfzone diffusivity variability and the parameterizations above [e.g., Bowen and Inman, 1974], the physical mechanism driving cross-shore diffusion was unclear.

[53] Mechanisms for cross-shore surfzone diffusion investigated here include bore-mixing, shear dispersion, and horizontal vortical-flow. Multiple cross-shore propagating bores with turbulent front faces (a high diffusivity region) can result in net cross-shore diffusion [Feddersen, 2007]. The non-dimensional bore-induced average diffusivity $\bar{\kappa}$ [Feddersen, 2007; Henderson, 2007] is

$$\bar{\kappa} = \frac{\sqrt{\pi}}{\hat{c}\hat{T}}, \quad (23)$$

where \hat{c} and \hat{T} are the non-dimensional phase speed and wave period, respectively. A dimensional mid-surfzone $\bar{\kappa}_{xx}$ can be derived from the scalings of Feddersen [2007]

$$\bar{\kappa}_{xx} = O(1) \frac{\sqrt{\pi} h^2}{T}. \quad (24)$$

[54] Assuming a self-similar surfzone ($H/h = \gamma$) and a mid-surfzone water depth ($h = h_b/2$) then

$$\bar{\kappa}_{xx} = O(1) \frac{\sqrt{\pi}}{4\gamma^2} H_b^2 T^{-1}. \quad (25)$$

[55] With $\gamma = 0.6$, the slope between κ_{xx} and $H_b^2 T^{-1}$ would be near 2.

[56] Here the incident (measured at frame 7, Figure 1) H_s and mean period T_m (Table 1) are used in the bore induced κ_{xx} scaling (25). Although observed κ_{xx} generally increase with $H_s^2 T_m^{-1}$ (Figure 13a), the correlation is low ($r^2 = 0.32$), and the best-fit slope of 11.7 is a factor 6 larger than expected for bore-induced dispersion (25). The observed cross-shore dye dispersion is probably not dominated by bore-mixing. However, the range of H_s and T_m are small (Table 1) and the κ_{xx} error bars (Figure 13a) often overlap, indicating the need for more observations.

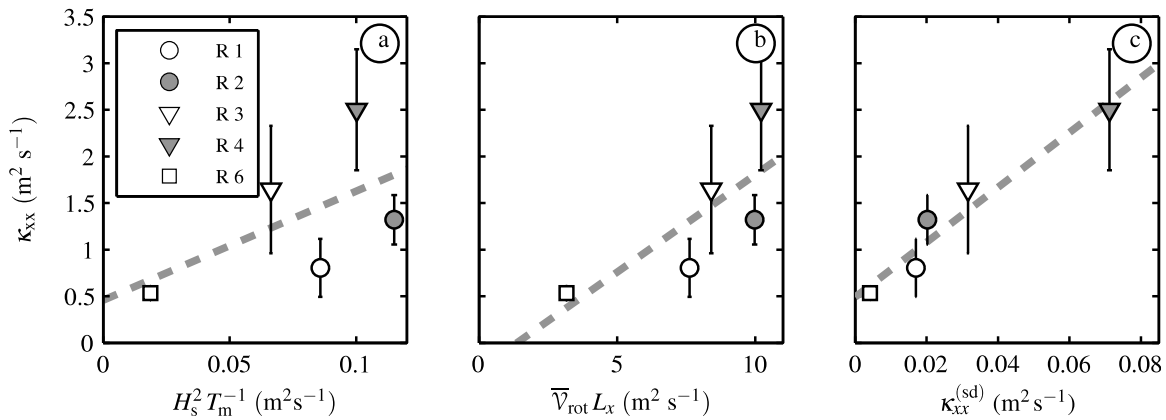


Figure 13. Estimated surfzone cross-shore diffusivity $\kappa_{xx} \pm \epsilon_{\kappa}$ versus (a) $H_s^2 T_m^{-1}$, (b) $\bar{V}_{rot} L_x$, and (c) $\kappa_{xx}^{(sd)}$. The fit slopes are 11.7 and 0.2, and r^2 correlations are 0.32 and 0.59 for $H_s^2 T_m^{-1}$ (Figure 13a) and $\bar{V}_{rot} L_x$ (Figure 13b), respectively. In Figure 13c, the $r^2 = 0.94$ correlation is high, but $\kappa_{xx}^{(sd)}$ magnitudes are much smaller than the observed κ_{xx} .

[57] In model simulations [Spydell and Feddersen, 2009], horizontal rotational velocities (i.e., vortical flow) generated by finite crest length breaking [Peregrine, 1998] or shear instabilities of the alongshore current [e.g., Oltman-Shay et al., 1989] were found to be a primary mixing mechanism. Here, a mixing-length scaling, i.e., a velocity scale times a length scale [e.g., Tennekes and Lumley, 1972], is examined using a surfzone width L_x length-scale and a surfzone-averaged low-frequency horizontal rotational velocity scale \bar{V}_{rot} (i.e., cross-shore averaged $V_{rot}(x)$ (1) between the shoreline and $x = -L_x$, Table 1)

$$\kappa_{xx} = \alpha \bar{V}_{rot} L_x \quad (26)$$

where α is a non-dimensional constant. In analogy with Von Kármán's constant of 0.4 in wall-bounded shear flow, or the factor of 0.57 [e.g., Rodi, 1987] in 2-equation (i.e., $k - \epsilon$) models relating diffusivity to a length- and velocity scale product, α is expected to be <1 but still $O(1)$. Surfzone $V_{rot}(x)$ includes horizontal rotational flow driven by instabilities in the alongshore current [e.g., Oltman-Shay et al., 1989], finite crest-length wave-breaking [Peregrine, 1998; Spydell and Feddersen, 2009], and wave groups [e.g., Reniers et al., 2004]. The surfzone averaged \bar{V}_{rot} ranges between 0.036–0.09 ms^{-1} (Table 1).

[58] The surfzone tracer κ_{xx} increase with $\bar{V}_{rot} L_x$ (Figure 13b) and the linear best-fit gives $r^2 = 0.59$, slope of 0.2, and near-zero y-intercept. The high r^2 and an expected slope <1 (for a mixing-length scaling) indicate that rotational velocities (surf-zone eddies) play an important role in cross-shore surfzone tracer mixing. However, similar to H_s and T_m , the range of \bar{V}_{rot} and L_x are relatively small (Table 1), and additional observations of surfzone tracer κ_{xx} are required to fully test this parameterization (26). A related mixing-length scaling, using \bar{V} instead of \bar{V}_{rot} as the velocity scale, was correlated with alongshore drifter diffusivity [Spydell et al., 2009], and is consistent with the present result because $V_{rot}(x)$ and V are correlated [Noyes et al., 2004].

[59] As suggested by Pearson et al. [2009], another possible mechanism for cross-shore surfzone tracer mixing is shear dispersion [e.g., Taylor, 1954] driven by vertical

variation of the cross-shore mean velocity (i.e., undertow). The idealized expression, assuming a step function velocity profile, for the shear dispersion driven $\kappa_{xx}^{(sd)}$ [Fischer, 1978] used by Pearson et al. [2009]

$$\kappa_{xx}^{(sd)} = \frac{(U_+ - U_-)^2 h^2}{48 \kappa_{zz}}, \quad (27)$$

where h is the water depth, κ_{zz} is the surfzone vertical diffusivity, U_+ and U_- are the cross-shore velocities in the surface (onshore) and return (offshore) layers with the transition at $h/2$. Other plausible velocity profiles (e.g., linear) have different functional forms for $\kappa_{xx}^{(sd)}$ [Fischer, 1978], but give similar results when the on-offshore transports are matched between profiles. Using (27) and empirical relationships for κ_{zz} and U_+ , and assuming $U_- = -U_+$, Pearson et al. [2009] found good agreement between a laboratory estimated κ_{xx} and the corresponding scaled $\kappa_{xx}^{(sd)}$ for shore-normal monochromatic waves.

[60] The cross-shore shear dispersion scaling (27) is examined with field data derived from the instrumented frames. During each release, U_- is given by mid-surfzone cross-shore velocities, measured at the instrumented frames (Figure 1) roughly 0.4 m above the bed in 1–2 m water depth. The maximum U_- is -0.07 ms^{-1} , and analogous to Pearson et al. [2009], $U_+ = -U_-$ is assumed. The vertical cross-shore velocity profile is unknown, however the step function profile assumed in (27) is used for comparison to previous work [Pearson et al., 2009]. At the same locations the estimated surfzone turbulent dissipation rate $\epsilon \approx 4 \times 10^{-4} \text{ m}^2 \text{ s}^{-3}$ (F. Feddersen, Quality controlling surfzone acoustic Doppler velocimeter observations to estimate the turbulent dissipation rate, submitted to *Journal of Atmospheric and Oceanic Technology*, 2010). Assuming a turbulent length-scale of half the water depth, the resulting κ_{zz} derived from a $k - \epsilon$ closure scheme [e.g., Rodi, 1987] are typically $\kappa_{zz} \approx 4 \times 10^{-2} \text{ m}^2 \text{ s}^{-1}$. A linear best-fit of κ_{xx} to $\kappa_{xx}^{(sd)}$ (Figure 13c) results in high correlation ($r^2 = 0.94$), but a large slope of 30. The $\kappa_{xx}^{(sd)}$ are expected to be $O(1)$ estimates of cross-shore shear dispersion, but ranged from 35–125 times smaller than the observed κ_{xx} (Figure 13c). If

vertical tracer gradients exist (section 6.4), the $\kappa_{xx}^{(sd)}$ may be underestimated, however this is unlikely to account for the large differences in magnitude. Although correlations are high, undertow driven cross-shore shear dispersion is apparently not a dominant tracer dispersal mechanism in the observed natural surfzone. In the laboratory, with monochromatic, shore-normal waves [Pearson *et al.*, 2009], horizontal rotational velocities are reduced or absent and the undertow driven shear dispersion mechanism may be dominant.

6.4. Potential Causes for Reduced Downstream $M(y_j)$ Relative to Dye Pump Estimates

[61] Tracer transports at the source $M(y = 0 \text{ m})$, estimated using the dye pump rate, are larger than at downstream transects $M(y > 0 \text{ m})$, estimated with the observed $\bar{D}(y_j)$, $V(x)$, and $h(x)$ (Figure 9). The reasons for the initial $M(y_j)$ decrease are unknown, but possible causes, and the implications of those causes on tracer analysis, are explored. One possibility is that pump rates were overestimated by using water (lower viscosity than dye) from a bucket (not the dye tank). However testing on a similar pump system (the original was no longer available) did not support this hypothesis. Pump rate errors would not effect cross-shore moments or κ_{xx} , but would affect the predicted tracer maxima $\bar{D}_{\max}^{(p)}$ (19) used for model data comparison (Figure 12a).

[62] Increased near-bed dye concentration (where the jet ski does not sample) relative to the surface may be a cause of the reduced downstream $M(y_j)$ relative to the pumped $M(y = 0 \text{ m})$. The injected dye, with concentration 2.1×10^8 ppb, has a specific gravity of 1.2. In a coastal or open-ocean environment, weak vertical mixing requires density adjustment of the dye to prevent it from sinking towards the bottom [e.g., Ledwell *et al.*, 2004]. In contrast, the surfzone is a region of vigorous vertical mixing, where sand (2.65 specific gravity) is frequently lifted off of the bed and suspended at sediment-water densities $>1.001 \rho$ (where ρ is the density of seawater) [e.g., Beach and Sternberg, 1996] despite grain settling velocities of roughly 0.03 ms^{-1} [e.g., Hallermeier, 1981]. Maximum tracer concentrations 1 m from the source are estimated at 10^4 ppb with a density of 1.0001ρ , based upon the conservative assumptions of a constant 0.1 m vertical dye layer (no vertical mixing), advected by $\bar{V} = 0.1 \text{ ms}^{-1}$ (Table 1) and a small-scale cross-shore diffusivity of $0.01 \text{ m}^2 \text{ s}^{-1}$ (from turbulent dissipation, section 6.3). Thus potential tracer induced stratification is considered negligible. With the conservative vertical diffusivity estimate $\kappa_{zz} = 10^{-2} \text{ m}^2 \text{ s}^{-1}$, mid-water column released dye in $h = 2 \text{ m}$ depth has a surface value $>90\%$ of the mid-depth maximum, for $t_p > 40 \text{ s}$, and is consistent with the visual observations of rapid vertical mixing. Thus, dye tracer is expected to be vertically well mixed at downstream transect locations.

[63] The region between x_{in} (Table 2) and the $x = 0$ shoreline ($\approx 10 \text{ m}$ wide) was not sampled by the jet ski or included in $M(y_j)$, and the excluded near-shoreline tracer transport is a potential cause of the low biased $M(y > 0 \text{ m})$ relative to the pump estimated $M(y = 0 \text{ m})$. The non-shoreline attached R1, with low shoreline dye concentrations, is not expected to have significant near-shoreline

transport, and indeed the $M(y_j)$ are roughly conserved from the release point to farther downstream (Figure 9a). Near-shoreline tracer transports are unknown, but qualitative estimates (not shown) are made assuming constant \bar{D} and V between x_{in} and the shoreline. For the two R2 transects closest to the release location, the qualitative near-shoreline estimates are consistent with the correction required to match transect $M(y > 0 \text{ m})$ with pump rate $M(y = 0 \text{ m})$. For R3, R4 and R6 transects with $y < 200 \text{ m}$, the near-shoreline estimates are between 20–33% of the correction required to match $M(y > 0 \text{ m})$ and $M(y = 0 \text{ m})$, and farther downstream the estimates are negligible. Thus, dye flux inshore of x_{in} may be significant at times, but does not fully explain the generally high bias of pump $M(y = 0 \text{ m})$. Using the shoreline bounded analytic solution (13), and neglecting the near-shoreline region (i.e., integrating from x_{in} instead of $x = 0 \text{ m}$), increases κ_{xx} roughly 14–20%. Thus, the κ_{xx} bias for excluding near shoreline tracer is generally low compared with other uncertainties (error bars in Figure 13).

[64] Other factors also induce $M(y_j)$ errors not accounted for in the estimated $M(y_j)$ uncertainties (error bars in Figure 9). The bathymetry and alongshore currents $V(x)$ are assumed perfectly alongshore uniform, and alongshore variations would increase $M(y_j)$ uncertainties. However, it is not clear that these assumptions can induce a bias.

7. Summary

[65] The cross-shore surfzone dispersion of a continuously released dye tracer in an alongshore current was observed during six dye releases. Tracer concentrations were measured on repeated cross-shore transects, at various alongshore distances from the dye source, with a unique GPS-tracked jet ski dye sampling platform. Tracer is advected with the mean alongshore current (i.e., downstream) forming plumes that become wider and more diluted with distance downstream. Mean cross-shore profiles $\bar{D}(x, y_j)$ often have concentration maxima at or near the shoreline (shoreline attached) with decreasing concentration offshore, qualitatively consistent with a half-Gaussian shape. At large downstream distances from the source, $\bar{D}(x, y_j)$ is approximately constant across the surfzone with decreasing concentrations farther seaward, consistent with much lower diffusivity seaward of, than within, the surfzone.

[66] Tracer alongshore transport $M(y_j)$ and surface-center of mass $\mu(y_j)$ are estimated from the $\bar{D}(x, y_j)$. The mean alongshore $M(y_j)$ is roughly conserved downstream of the dye source, and is typically a factor of 2 smaller than the injected dye flux. For shoreline attached profiles the $\mu(y_j)$ move offshore with downstream distance. For shoreline attached profiles (R2–R6) the offshore μ movement with increasing y is associated with plume widening and not seaward advection of the mean plume.

[67] Surfzone cross-shore absolute diffusivities ($\kappa_{xx} = 0.5\text{--}2.5 \text{ m}^2 \text{ s}^{-1}$), based upon a simple Fickian diffusion model near a boundary, are estimated from mean $\bar{D}(x, y_j)$ profiles. To estimate surfzone diffusivity, only mean tracer transects where tracer is surfzone-contained are included in κ_{xx} fits. For shoreline attached profiles, the estimated diffusivities, the observed tracer surface-center of mass, and

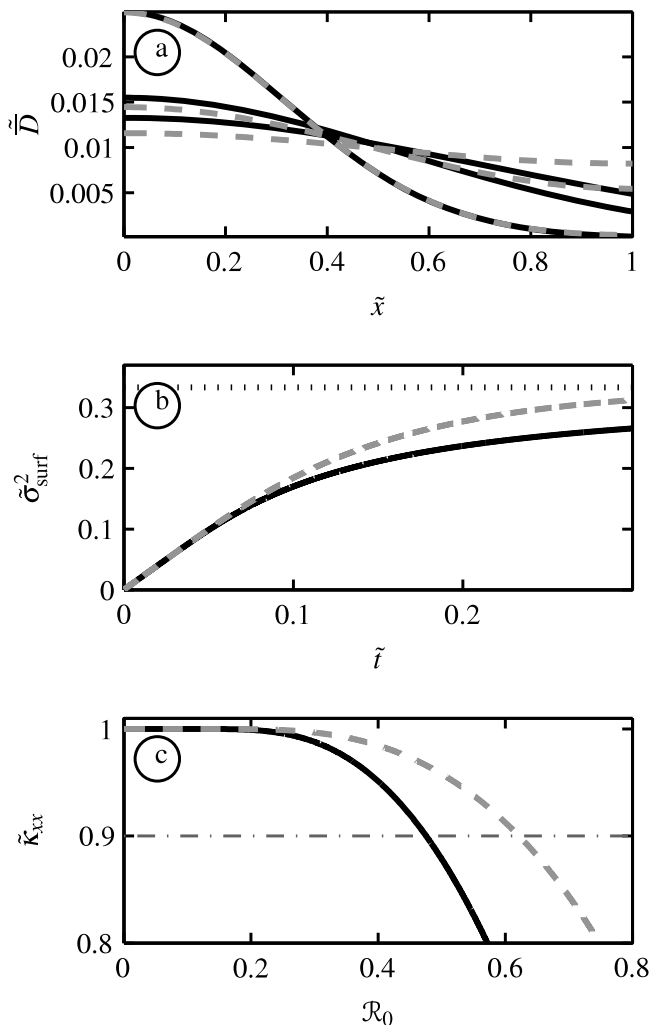


Figure B1. (a) Modeled non-dimensional dye concentration \bar{D} versus non-dimensional \tilde{x} at three times ($\tilde{t} = 0.05, 0.15, 0.25$), for (black curves) diffusion on a semi-infinite domain (no-flux boundary at $\tilde{x} = 0$) where the \bar{D} are truncated at $\tilde{x} = 1$, and (dashed grey curves) diffusion on a closed $0 < \tilde{x} < 1$ domain with no-flux boundaries. (b) Non-dimensionalized $\tilde{\sigma}_{\text{surf}}^2$ versus non-dimensionalized \tilde{t} , with saturated $\tilde{\sigma}_{\text{surf}}^2 = 1/3$ (dotted curve) for reference. (c) Non-dimensional fit $\tilde{\kappa}_{xx}$ (using $\tilde{\sigma}_{\text{surf}}^2$ with $0 < \mathcal{R} < \mathcal{R}_0$) versus \mathcal{R}_0 and, (dot-dashed curve) the $\tilde{\kappa}_{xx} = 0.9$ threshold used to determine the \mathcal{R}_0 cutoff.

the observed tracer maxima are all consistent with the Fickian modeled half-Gaussian solution.

[68] Three potential mechanisms for cross-shore tracer dispersion in the surfzone are examined by testing cross-shore diffusivity parameterizations. A breaking-wave induced κ_{xx} parameterization has low correlation with observed κ_{xx} ($r^2 = 0.32$), and the best-fit slope is larger than expected. Undertow driven shear dispersion estimates have high correlation ($r^2 = 0.94$), but significantly under-predict the observed κ_{xx} , indicating that this mechanism is not a dominant term in cross-shore surfzone tracer dispersion. A mixing-length parameterization based on 2D horizontal

rotational velocities (surfzone eddies) with length-scales of the surfzone width or less has good correlation ($r^2 = 0.59$) and a best-fit slope < 1 (as expected). This suggests that the observed tracer dispersion is primarily due to surfzone eddies forced either by shear instabilities (shear waves) or by finite-crest-length wave breaking.

[69] The reasons for the decreased alongshore tracer transport $M(y_j)$, relative to pump rate estimates, are unknown and possible causes are examined. Tracer induced stratification is estimated to be negligible, and unlikely to explain the $M(y_j)$ decrease. Tracer transport in the neglected near-shoreline region (where the jet ski does not sample) is generally not large enough to account for the $M(y_j)$ decrease. Neglecting tracer near the shoreline may bias κ_{xx} estimates up to 20%.

Appendix A: Degrees of Freedom in Estimating $\bar{D}(x, y_j)$

[70] For each release, the degrees of freedom \mathcal{N}_j at each y_j are estimated from the Eulerian decorrelation time τ_{decorr} and the times between transect realizations. Surfzone dye concentration time series (not shown), measured by fluorimeters [Clark *et al.*, 2009] mounted on the instrumented frames (Figure 1), are used to estimate $\tau_{\text{decorr}} = A(0)^{-1} \int_0^{\tau_{\text{max}}} A(\tau) d\tau$ [e.g., Emery and Thomson, 2001], where $A(\tau)$ is the lagged (τ) dye concentration autocorrelation function and τ_{max} is the maximum lag (roughly the duration of each dye release). Sequential D_i realizations separated by times greater than τ_{decorr} are assumed independent and add one to \mathcal{N}_j . A group of realizations separated by times less than τ_{decorr} are assumed fractionally independent and add $1 + (\bar{t}_b - \bar{t}_a)\tau_{\text{decorr}}^{-1}$ to \mathcal{N}_j , where \bar{t}_a and \bar{t}_b are the mean times of the first and last realizations in the group. The resulting \mathcal{N}_j is between 1 and number of realizations N_j (Table 2).

Appendix B: Surfzone Saturation Ratio for Estimating κ_{xx}

[71] Estimates of $\sigma_{\text{surf}}^2(y_j)$ are only included in cross-shore surfzone diffusivity κ_{xx} fits (14) if the mean tracer is surfzone contained, so that the fit κ_{xx} represents surfzone diffusivity rather than a combination of the surfzone and the region seaward. To quantify which transects are well contained in the surfzone, a surfzone saturation ratio \mathcal{R} (17) is defined as the ratio of $\sigma_{\text{surf}}^2(y_j)$, to the σ_{surf}^2 value for uniform tracer across the surfzone (i.e., saturated). The threshold \mathcal{R}_0 for determining which y_j locations to include in κ_{xx} fits is developed for shoreline attached profiles (the majority of observations) by modeled tracer diffusion.

[72] The surfzone is likely a region of high diffusivity with lower diffusivity seaward. The transition between these two regions is not understood. Thus, two possible extremes for tracer diffusion are considered to determine the \mathcal{R} threshold. The first is constant diffusivity on a semi-infinite domain with a shoreline no-flux boundary. The second is constant diffusivity within the surfzone (width L_x) with zero diffusivity seaward. This is modeled as a closed domain with no-flux boundaries at the shoreline and the seaward surfzone edge. Diffusivity along the seaward edge of the surfzone is somewhere in between these two extremes.

[73] Non-dimensional variables are introduced

$$\begin{aligned}\tilde{x} &= \frac{x}{L_x}, \\ \tilde{t} &= \frac{t\kappa_{xx}}{L_x^2}, \\ \tilde{D} &= \frac{\bar{D}}{\int_0^1 \bar{D} d\tilde{x}}, \\ \tilde{\sigma}_{\text{surf}} &= \frac{\sigma_{\text{surf}}}{L_x}, \\ \tilde{\kappa}_{xx} &= \frac{1}{2} \frac{d\tilde{\sigma}_{\text{surf}}^2}{d\tilde{t}},\end{aligned}$$

and result in the non-dimensional diffusion equation with a delta function source at the shoreline

$$\frac{\partial \tilde{D}}{\partial \tilde{t}} = \tilde{\kappa}_{xx} \frac{\partial^2 \tilde{D}}{\partial \tilde{x}^2} + \delta(\tilde{x} = 0, \tilde{t} = 0),$$

solved on the semi-infinite and closed domains described above. \bar{D} profiles (Figure B1a) are initially Gaussian until \bar{D} reaches $\tilde{x} = 1$ and either moves beyond the surfzone (semi-infinite domain) or interacts with the surfzone boundary (closed domain). The closed domain increases dye concentrations in the outer surfzone (Figure B1a), resulting in larger closed domain $\tilde{\sigma}_{\text{surf}}^2$ relative to the semi-infinite domain (Figure B1b). The $\tilde{\sigma}_{\text{surf}}^2$ are linear with respect to \tilde{t} for $\tilde{t} < 0.05$, but asymptotically approach the surfzone saturation limit $[\tilde{\sigma}_{\text{surf}}]^2 = 1/3$ for large \tilde{t} (Figure B1b). Fitting $\tilde{\kappa}_{xx}$ to $\tilde{\sigma}_{\text{surf}}^2$ for $\tilde{t} < 0.05$, where $\tilde{\sigma}_{\text{surf}}^2$ growth is linear (Figure B1b), produces the correct $\tilde{\kappa}_{xx} = 1$ (Figure B1c). Including data with $\tilde{t} > 0.05$, where the $\tilde{\sigma}_{\text{surf}}^2$ growth rate decreases, reduces the fit $\tilde{\kappa}_{xx}$ from the true value (Figure B1c).

[74] The greatest possible number of field σ_{surf}^2 should be used to estimate κ_{xx} without significantly biasing κ_{xx} from the surfzone value. Requiring that the fit $\tilde{\kappa}_{xx} \geq 0.9$ gives the threshold $\mathcal{R}_0 = 0.48$ and $\mathcal{R}_0 = 0.62$ for the semi-infinite and closed domains, respectively (Figure B1c), with average $\mathcal{R}_0 = 0.55$. Only transects between the dye source ($y = 0$ m) and the farthest downstream transect where $\mathcal{R} < \mathcal{R}_0$ are included in κ_{xx} fits (black symbols, Figures 11b–11f).

[75] **Acknowledgments.** This research was supported by CA Coastal Conservancy, NOAA, NSF, ONR, and CA Sea Grant. Staff, students, and volunteers from the Integrative Oceanography Division (B. Woodward, B. Boyd, K. Smith, D. Damell, I. Nagy, M. Omand, M. Yates, M. McKenna, M. Rippey, S. Henderson, D. Michrokowski) were instrumental in acquiring these field observations. We thank these people and organizations.

References

Batchelor, G. K. (1949), Diffusion in a field of homogeneous turbulence. I. Eulerian analysis, *Aust. J. Sci. Res. Ser. A*, *2*, 437–450.
 Batchelor, G. K. (1952), Diffusion in a field of homogeneous turbulence. II. The relative motion of particles, *Proc. Cambridge Philos. Soc.*, *48*, 345–363.
 Beach, R. A., and R. W. Sternberg (1996), Suspended-sediment transport in the surf zone: Response to breaking waves, *Cont. Shelf Res.*, *16*, 1989–2003.
 Boehm, A. B., S. B. Grant, J. H. Kim, C. D. McGee, S. Mowbray, C. Clark, D. Foley, and D. Wellmann (2002), Decadal and shorter period variability of surfzone water quality at Huntington Beach, California, *Environ. Sci. Technol.*, *36*, 3885–3892.
 Bowen, A. J., and D. L. Inman (1974), Nearshore mixing due to waves and wave-induced currents, *Rapp. P. V. Reun. Cons. Int. Explor. Mer*, *167*, 6–12.

Brown, J., J. MacMahan, A. Reneirs, and E. B. Thornton (2009), Surfzone diffusivity on a rip channel beach, *J. Geophys. Res.*, *114*, C11015, doi:10.1029/2008JC005158.
 Clark, D. B., F. Feddersen, M. M. Omand, and R. T. Guza (2009), Measuring fluorescent dye in the bubbly and sediment laden surfzone, *Water Air Soil Pollut.*, *204*(1–4), 103–115, doi:10.1007/s11270-009-0030-z.
 Clarke, L. B., D. Ackerman, and J. Largier (2007), Dye dispersion in the surfzone: Measurements and simple models, *Cont. Shelf Res.*, *27*, 650–669.
 Csanady, G. T. (1973), *Turbulent Diffusion in the Environment*, D. Reidel, New York.
 Emery, W. J., and R. E. Thomson (2001), *Data Analysis Methods in Physical Oceanography*, Elsevier, New York.
 Feddersen, F. (2007), Breaking wave induced cross-shore tracer dispersion in the surfzone: Model results and scalings, *J. Geophys. Res.*, *112*, C09012, doi:10.1029/2006JC004006.
 Fischer, H. B. (1978), On the tensor form of bulk dispersion coefficient in a bounded skewed shear-flow, *J. Geophys. Res.*, *83*, 2373–2375.
 Fong, D. A., and M. T. Stacey (2003), Horizontal dispersion of a near-bed coastal plume, *J. Fluid Mech.*, *489*, 239–267.
 Grant, S. B., J. H. Kim, B. H. Jones, S. A. Jenkins, J. Wasyl, and C. Cudaback (2005), Surf zone entrainment, along-shore transport, and human health implications of pollution from tidal outlets, *J. Geophys. Res.*, *110*, C10025, doi:10.1029/2004JC002401.
 Haile, R. W., et al. (1999), The health effects of swimming in ocean water contaminated by storm drain runoff, *Epidemiology*, *10*, 355–363.
 Hallermeier, R. J. (1981), Terminal settling velocity of commonly occurring sand grains, *Sedimentology*, *28*, 859–865, doi:10.1111/j.1365-3091.1981.tb01948.x.
 Hanemann, M., L. Pendleton, and D. Layton (2001), Southern California beach valuation project: Summary report on the expenditure module, technical report, Natl. Oceanic and Atmos. Admin., Silver Spring, Md. (Available at <http://marineconomics.noaa.gov/scbeach/laobeach1.html>).
 Harris, T. F. W., J. M. Jordaan, W. R. McMurray, C. J. Verwey, and F. P. Anderson (1963), Mixing in the surf zone, *Air Water Pollut.*, *7*, 649–667.
 Henderson, S. M. (2007), Comment on “Breaking wave induced cross-shore tracer dispersion in the surfzone: Model results and scalings”, *J. Geophys. Res.*, *111*, C12007, doi:10.1029/2006JC003539.
 Inman, D. L., R. J. Tait, and C. E. Nordstrom (1971), Mixing in the surfzone, *J. Geophys. Res.*, *26*, 3493–3514.
 Johnson, D., and C. Pattiaratchi (2004), Transient rip currents and near-shore circulation on a swell-dominated beach, *J. Geophys. Res.*, *109*, C02026, doi:10.1029/2003JC001798.
 Johnson, D., and C. Pattiaratchi (2006), Boussinesq modelling of transient rip currents, *Coastal Eng.*, *53*(5), 419–439.
 Jones, N. L., R. J. Lowe, G. Pawlak, D. A. Fong, and S. G. Monismith (2008), Plume dispersion on a fringing coral reef system, *Limnol. Oceanogr.*, *53*(20), 2273–2286.
 Ledwell, J. R., T. F. Duda, M. A. Sundermeyer, and H. E. Seim (2004), Mixing in a coastal environment: 1. A view from dye dispersion, *J. Geophys. Res.*, *109*, C10013, doi:10.1029/2003JC002194.
 Lippmann, T. C., T. H. C. Herbers, and E. B. Thornton (1999), Gravity and shear wave contributions to nearshore infragravity motions, *J. Phys. Oceanogr.*, *29*(2), 231–239.
 Noble, R. T., J. H. Dorsey, M. Leecaster, V. Orozco-Borbón, D. Reid, K. Schiff, and S. B. Weisberg (2000), A regional survey of the microbiological water quality along the shoreline of the Southern California Bight, *Environ. Monit. Assess.*, *64*(1), 435–447.
 Noyes, T., R. Guza, S. Elgar, and T. Herbers (2002), Comparison of methods for estimating nearshore shear wave variance, *J. Atmos. Oceanic Technol.*, *19*(1), 136–143.
 Noyes, T., R. Guza, S. Elgar, and T. Herbers (2004), Field observations of shear waves in the surf zone, *J. Geophys. Res.*, *109*, C01031, doi:10.1029/2002JC001761.
 Oltman-Shay, J., P. A. Howd, and W. A. Birkemeier (1989), Shear instabilities of the mean longshore current: 2. Field observations, *J. Geophys. Res.*, *94*, 18,031–18,042.
 Pearson, J. M., I. Guymer, J. R. West, and L. E. Coates (2009), Solute mixing in the surf zone, *J. Waterw. Port Coastal Ocean Eng.*, *135*(4), 127–134.
 Peregrine, D. H. (1998), Surf zone currents, *Theor. Comput. Fluid Dyn.*, *10*, 295–309.
 Reniers, A., J. Roelvink, and E. Thornton (2004), Morphodynamic modeling of an embayed beach under wave group forcing, *J. Geophys. Res.*, *109*, C01030, doi:10.1029/2002JC001586.
 Rodi, W. (1987), Examples of calculation methods for flow and mixing in stratified fluids, *J. Geophys. Res.*, *92*, 5305–5328.
 Seymour, R., R. Guza, W. O’Reilly, and S. Elgar (2005), Rapid erosion of a small Southern California beach fill, *Coastal Eng.*, *52*(2), 151–158.

- Spydell, M. S., and F. Feddersen (2009), Lagrangian drifter dispersion in the surf zone: Directionally spread, normally incident waves, *J. Phys. Oceanogr.*, *39*, 809–830.
- Spydell, M. S., F. Feddersen, R. T. Guza, and W. E. Schmidt (2007), Observing surf-zone dispersion with drifters, *J. Phys. Oceanogr.*, *37*(12), 2920–2939.
- Spydell, M. S., F. Feddersen, and R. T. Guza (2009), Observations of drifter dispersion in the surfzone: The effect of sheared alongshore currents, *J. Geophys. Res.*, *114*, C07028, doi:10.1029/2009JC005328.
- Taylor, G. I. (1921), Diffusion by continuous movements, *Proc. London Math. Soc.*, *20*, 196–212.
- Taylor, G. (1954), The dispersion of matter in turbulent flow through a pipe, *Proc. R. Soc. London A*, *223*(1155), 446–468.
- Tennekes, H., and J. L. Lumley (1972), *A First Course in Turbulence*, MIT Press, Cambridge, Mass.
- Wunsch, C. (1996), *The Ocean Circulation Inverse Problem*, Cambridge Univ. Press, Cambridge, U. K.
-
- D. B. Clark, F. Feddersen, and R. T. Guza, Integrative Oceanography Division, Scripps Institution of Oceanography, University of California San Diego, 9500 Gilman Dr., Mail Code 0209, La Jolla, CA 92093, USA. (d2clark@ucsd.edu)